Development and validation of an Alaskan coupled storm surge, tide, wind wave, and sea ice forecasting system

Guoming Ling [a,b], Damrongsak Wirasaet [a], Joannes J. Westerink [a], María Teresa Contreras Vargas [a], Mindo Choi [a], William J. Pringle [c], Coleman Blakely [a], David H. Richter [a], Ali Abdolali [d,e], Andre van der Westhuysen [d,e], Kyle R. Steffen [f], Clint Dawson [f], Ayumi Fujisaki-Manome [g], Jia Wang [g], Edward Myers [e], Saeed Moghimi [e], Carol Janzen [g], Rob Bochenek [g], Jesse Lopez [g]

[a] *Department of Civil and Environmental Engineering and Earth Sciences, University of Notre Dame, IN, USA*

[b] *International Research Institute of Disaster Science (IRIDeS), Tohoku University, Sendai, Japan*

[c] *Environmental Science Division, Argonne National Laboratory, Lemont, IL, USA*

[d] *NWS/NCEP/Environmental Modeling Center, National Oceanic and Atmospheric Administration (NOAA), College Park, MD, USA*

[e] *NOAA National Ocean Service, Office of Coast Survey (NOAA/OCS)*

[f] *University of Texas at Austin*

[g] *Great Lakes Environmental Research Laboratory (NOAA GLERL)*

Corresponding author: Guoming Ling, ling@irides.tohoku.ac.jp

ABSTRACT: Western Alaska regularly experiences storm surge events induced by extra-tropical storms, most active during fall, winter, and spring. Among others, the presence of sea ice in Western Alaska seawater poses a challenge in modeling storm surge in this area. Existing storm surge models rarely consider sea ice effects together with wind-induced wave effects. In this paper, we present an ALaska Coastal Ocean Forecast System (ALCOFS) which considers sea ice and wave effects for a real time storm tide forecasting. The system is based on a tightly coupled ADCIRC (a hydrodynamics model used widely for tide and storm surge modeling based on shallow water equations) and SWAN (wind wave model governed by spectrum action balance equation). The sea ice effect is included by incorporating a parameterization of air-sea-ice drag in the ADCIRC storm surge model, and of the wave energy dissipation caused by sea ice is considered in SWAN. The model utilizes an unstructured mesh with variable resolution (ranging from 20km to 70m) to achieve accurate predictions and fast run times. The model was exercised carefully with tidal tests to obtain good quality of tidal results and the optimized parameter setups. The impact of sea ice and waves was examined with several storm surge events. In addition, a three year long storm surge hindcast has been conducted to test the model robustness and to examine the sea level variation trends. Furthermore, an efficient real time continuous storm tide, wave and surge forecasting scheme which performs a cycle with a one day nowcast and then a five day forecast is proposed. The performance of the forecasting system is demonstrated and evaluated through a year long forecast. To examine the effectiveness of the forecasting scheme, it is demonstrated through the SWAN+ADICRC and stand alone WAVEWATCH III (WWIII) models. The recorded forecast results for the past show good performance by comparing with observations. This paper underscores the importance of incorporating sea ice and wave effects into simulations of storm surges for the area with sea ice conditions, and presents the skill of the forecasting system.

1. Introduction

The western Alaska coast has experienced numerous storm surge events resulting from regular intense storms occurred in the Chukchi and Bering Sea. For example, the largest storm in November 1974 resulted in maximum water level as high as 4 m above mean lower low water level (MLLW) in Nome, with an estimated $12-15 million damages to the city (Blier et al. 1997; Fathauer 1975). A comparable storm in November 2011 resulted in measured storm tide elevation 3.3 m above MSL (approximately 50 cm greater than the peak water elevation documented by the NOAA tide gauge), with estimated $29.9 million damages to 37 cities and villages (Kinsman and DeRaps 2012). There are more recent storms with smaller surge height (around 2 m above MSL at Nome) occurred in February 2011, January 2017, February 2019. These events generally occurred during the winter with the presence of sea ice, which indicates the importance of considering the sea ice effects to tides, surge and waves. In a previous study, Joyce et al. (2019) incorporated the sea ice effect on surge through parameterizations of the wind drag coefficient, modifying the air-sea momentum transfer for the area with ice coverage. As a result, the proposed model was able to reduced the peak surge errors at the investigated stations compared to the model without sea ice effect. However, there are still some uncertainties in the model such as the lack of considering waves and their interaction with surge and ice (Joyce et al. 2019). In addition, this high-resolution Alaska model (coastal resolution ~25 m) contains 4.1 million nodes with similar high resolution in the deep ocean which turns out to be inefficient for a rapid real time operational forecasting with limited computer resources.

In this regard, to further investigate the combined impact of sea ice, tides, storm waves and surge along the western Alaska coast, we incorporate a more comprehensive 'air-sea-ice drag' parameterization which considers the effect of ice floe size. In addition, we activate the ice functionality in the state-of-the-art tightly coupled wave and surge model, the Simulating WAves Nearshore (SWAN) and the ADvanced CIRCulation (ADCIRC) model (ADCIRC-SWAN; Dietrich et al. 2011).

At the same time, the design of mesh resolution acts as an important role to affect the computational accuracy and the efficiency, we applied a MATLAB-based mesh generator OceanMesh2D (Roberts et al. 2019a,b) which targeted the fine resolution in narrow geometric features, along steep topographic gradients, along pronounced submerged estuarine channels, and floodplains with local communities, while aggressively relaxing resolution elsewhere especially in the deep ocean area. By this approach, we reduced the node number to 1.6 million which leads to 8 times faster than the previous study high resolution mesh (Joyce et al. 2019). In addition, high fidelity bathymetry database especially over the continental shelves in coastal areas plays an important role to accurately predicting both waves and surge (Provost and Lyard 2003; Weaver and Slinn 2010). For this consideration, we blended the current available bathymetries with GEBCO2020, the Smooth Sheet bathymetries of Aleutian Islands, Cook Inlet, Central Gulf of Alaska, Norton Sound, the Southern Alaska Coastal Relief Model (CRM) bathymetry and the NOAA chart bathymetry (US4AK85M).

In this paper, we present a real time operational forecasting approach for the storm wave and surge prediction. The approach is applied to develop an ALaska Coastal Ocean Forecast System (ALCOFS), in this system, the SWAN+ADCIRC model works as the main engine, which couples wave, surge models and sea ice in the northern Pacific Ocean, Bering, Chukchi and Arctic Seas. In order to get as accurate the model as we could, we first perform the parameterizations of internal tide and bottom friction for the tidal analysis, then we validate the air-sea-ice formulation and wave-surge-ice interaction by comparing to observations, stand-alone ADCIRC model without forcing ice and stand-alone ADCIRC model with ice forcing for several past storms. Also, we implement a three year long term hindcast to coordinate the uncertainties about the sea level trends. Finally, we evaluate the ALCOFS recording results for the past one year forecast with observations. And in order to see the forecasted wave performance, we also compare the wave results from SWAN with a regional WAVEWATCH III® (WWIII) (WW3DG 2019) and a global WWIII models.

This paper is organized as follows. Section 2 gives a brief introduction of ADCIRC, incorporation of sea ice drag parameterization, ADCIRC+SWAN coupled model with ice activation, introduction of a storm surge forecasting system, and the operational model. Section 3 shows the validation of tidal simulation for the operational model. Section 4 presents the numerical experiments with sea ice. Section 5 presents the numerical experiments with wave effects. Investigation of long term hindcast is presented in Section 6. The forecast results are validated in the Section 7. The conclusion of this study and a discussion of the results are given in Section 8.

2. Methodology

a. ADCIRC version 55

ADvanced CIRCulation (ADCIRC) is a finite element hydrodynamic model that is widely used for simulating hurricane storm surge, tides, and coastal circulation problems (Westerink et al. 2008). ADCIRC is based on the shallow water equations. In 2D mode, it solves the so-called generalized wave continuity equation, a reformulation of the primitive continuity equation, and the depth-averaged momentum equations for both water surface elevation and the depth-averaged velocity field. Since our model domain encompasses large areas (see Section e below), we consider the governing equations in spherical coordinates (see Kolar et al. (1994) *CITE theory and report* for detailed account on the governing equations and numerical implementation please). We employ ADCIRC version 55 which contains, among other upgrades, revision in the implementation of the model formulation in spherical coordinates for global domain modelling (Pringle et al. 2021). Such revision includes terms, previously omitted in prior versions, that are negligible for domain but become important at high-latitude. Forcings driven flow include tidal forcing and surface wind stresses.

The surface wind stress is computed using the quadratic drag formula: with the index notation,

$$\tau_{si} = \rho_a C_{\mathrm{d}} U_{10i} \sqrt{U_{10j} U_{10j}}, \tag{1}$$

where U_{10i}, U_{10j} are the neutral stability 10 m wind speed in the i, j horizontal directions (east-west and south-north), ρ_a is the density of air and C_{d} is the drag coefficient defining the air-sea momentum transfer. Here, the effect of sea ice is taken into account in the drag coefficient. For the ice free condition C_{d} corresponds to $C_{\mathrm{d,w}}$, the air-sea drag coefficient which is computed by using the Garratt's drag formula (Garratt 1977) limited to an upper bound of 0.0025 to represent sheeting of waves at high wind speeds (>27m/s):

$$C_{\mathrm{d,w}} = \min(2.5, 0.75 + 0.067\sqrt{U_{10j} U_{10j}}) \times 10^{-3}. \tag{2}$$

b. Parameterization for the sea ice effects

In the previous study, Joyce et al. (2019) incorporated the sea ice effect through a parameterization of the drag coefficient that considers both form and skin drag over the ice floe (Lüpkes and Birnbaum 2005) into ADCIRC model:

$$C_{\text{dn10}} = (1-A)C_{\text{d,w}} + AC_{\text{d,i}} + C_{\text{d,f}}, \tag{3}$$

where A denotes the sea ice concentration (the ice-covered area per unit area) whose value ranges from 0 (ice free) to 1 (fully covered), $C_{\text{d,i}}$ is the skin drag coefficient over sea ice, and $C_{\text{d,f}}$ is the form drag coefficient accounting the additional drag caused by the edges of floes. Joyce et al. (2019) used a constant $C_{\text{d,i}}$ of 0.0015 which was suggested in Lüpkes et al. (2012) based on the measurements conducting at the northeastern part of Fram Strait and the inner summer Arctic. Based on Lüpkes et al. (2012), Joyce et al. (2019) considered the form drag coefficient $C_{\text{d,f}}$ that is a semi-parabolic function of A:

$$C_{\text{d,f}} = 4C_{\text{d,f,max}}A(1-A), \tag{4}$$

where $C_{\text{d,f,max}}$ is set 0.0025, which is the maximum value of $C_{\text{d,f}}$ when $A = 0.5$. Equation 4 is able to represent the upper bound of the field measurements showed in Lüpkes et al. (2012), see Fig. 1. This formula is simple and yields satisfactory numerical results demonstrated therein. However, there is no possibility to take into account physical conditions, for examples, rougher or smoother, larger or smaller ice.

In this work, we consider the parameterized formulas of the form drag $C_{\text{d,f}}$ proposed by Lüpkes et al. (2012) which take into account ice conditions with different levels of approximations. The level 1 is the most complex background model which needs the information of ice concentration, ice thickness (or volume) and floe length. The level 2 formulation needs the ice concentration and freeboard; the level 3 formula simplifies level 2 by using a constant freeboard. The level 4 is the most simplified formula, which parameterized $C_{\text{d,f}}$ as a function of A with a tuning parameter representing floe sizes:

$$C_{\text{d,f}} = 3.67\times10^{-3}(1-A)^{\beta}A. \tag{5}$$

In the above formula, β is a tuning constant between 0.2 and 1.8 (smaller β is equivalent to smaller floe sizes which results in higher form drag). In our study, we tested level 2 and level 4 formulas, and that both yields very similar results. Therefore, the level 4 formula is adopted mainly because of its low computational cost. In addition, $\beta = 0.6$ (the light blue solid line in Fig. 1) tends to be able to represent most of the ice conditions compared to the observational data (the trend when A<0.5 and high value around A=0.7~0.8), the error statistics in APPENDIX B also show that $\beta = 0.6$ is the best choice compared to $\beta = 1.0$ and $\beta = 0.3$.

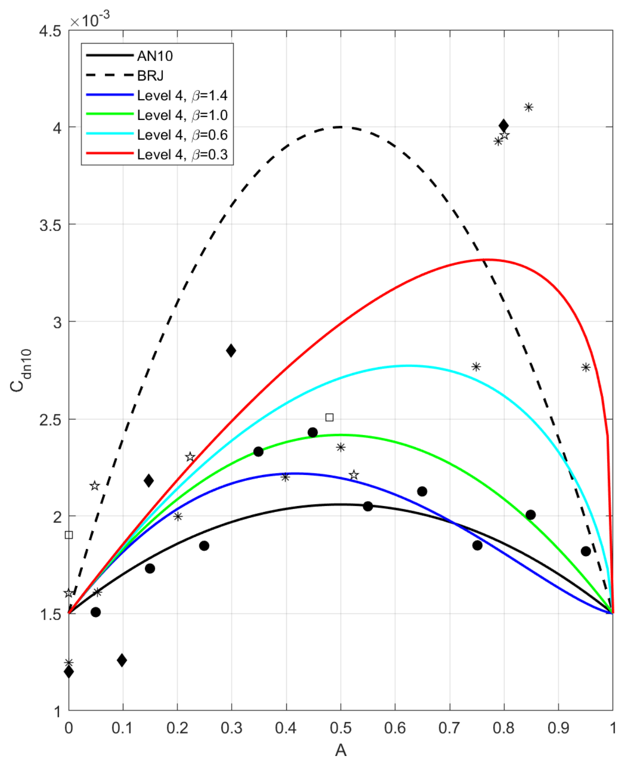

FIG. 1: Drag coefficients as a function of the sea ice concentration A. Symbols represent observations from different campaigns extracted from Lüpkes et al. (2012). Stars: MIZEX (Guest and Davidson (1987)); asterisks: MIZEX (Anderson (1987)); circles: REFLEX data; squares: REFLEX (Schröder et al. (2003)); diamonds: Antartic MIZ (Andreas et al. (1984)); black solid line: AN10 (Andreas et al. (2010)); black dash line: BRJ (Joyce et al. (2019)); color solid lines: Equations 3 and 5 with different β.

c. SWAN model

The Simulating WAves Nearshore (SWAN) (Booij et al. 1999) is a widely used third generation wave model based on the spectral action balance equation. Recently, Rogers (2019) incorporated the sea ice effect in the SWAN model through an implementation of a dissipation source term of the so-called 'IC4M2' method developed by Collins and Rogers (2017) for WAVEWATCH III to dissipate wave energy by sea ice. Note that the formula of this method is based on the polynomial fit of observation-based dissipation rates:

$$k_i = C_0 f^0 + C_1 f^1 + \cdots + C_6 f^6. \tag{6}$$

Here k_i (1/m) is the linear exponential attenuation rate of wave amplitude in space for the sea ice source term, f (Hz) is the frequency, and $C_{0,1,\ldots,6} = [0, 0, 1.06e-3, 0, 2.30e-2, 0, 0]$ are coefficients from a polynomial fit of data measured in the Antarctic marginal ice zone (Meylan et al. 2014).

d. Sea ice in SWAN + ADCIRC coupled model

A number of previous studies have shown the non-negligible effect for the contribution of wave-induced radiation stress to the water elevation of storm surge simulations during the hurricanes/storms (Dietrich et al. 2012; Xie et al. 2016; Li et al. 2020) (note that contribution of wind wave on the flow is carried out through an inclusion of the gradients of the wave radiation stress in the governing equations). To consider a two-way interaction between wind-driven waves and circulation, Dietrich et al. (2011) integrated the SWAN spectral wave model and ADCIRC shallow-water circulation model into a tightly-coupled SWAN+ADCIRC model. In the model, ADCIRC passes water levels and currents to SWAN and SWAN passes radiation stresses to ADCIRC. In this work, we enabled the recently-implemented IC4M2 in the ADCIRC+SWAN model system. The user command 'ADCICE' in SWAN is implemented to instruct the coupling system to activate the IC4M2 method in SWAN with sea ice concentration exported from ADCIRC.

e. Model mesh and setups

The model domain covers areas from the north Pacific Ocean to the Arctic Ocean, including the Gulf of Alaska, Bering Sea, Chukchi Sea, and Beaufort Sea, and floodplains along the coast of Western Alaska (see Figure 2). It consists of two curved open ocean boundaries on which the combination of the tidal elevation and the inverted barometer are prescribed (the later is employed in simulations with atmospheric forcings); the northern boundary is in the Arctic Ocean and the southern boundary in the Northern Pacific Ocean. These open boundaries are selected so that they traverse primarily through deep water areas to reduce the influence of the nonlinear tide. The

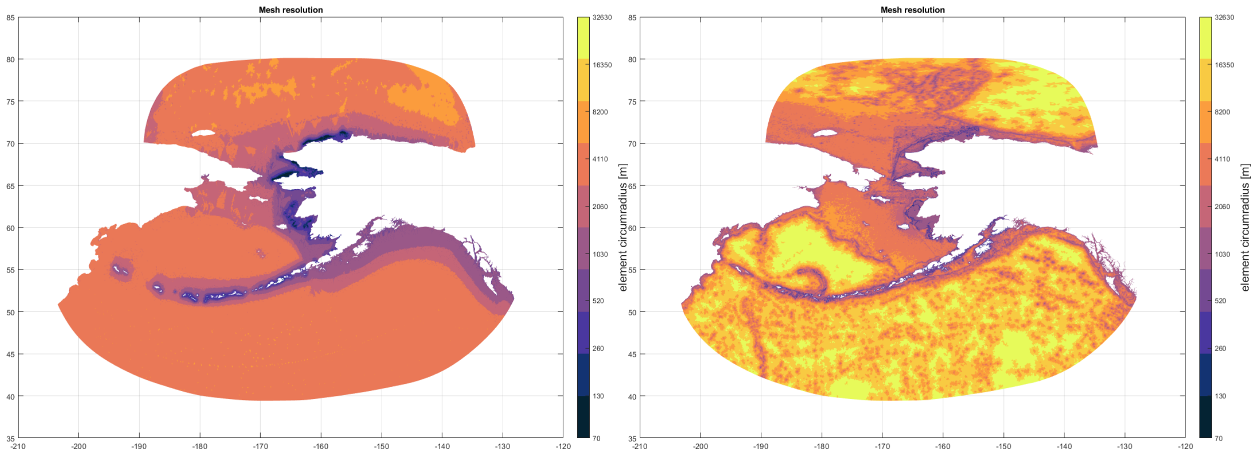

(a) High resolution model (b) Present operational model

FIG. 2: Comparison of the mesh resolutions. (a): High resolution model, resolution from 5,000 m to 25 m, 4.1 million nodes (Joyce et al. 2019); (b): Present operational model, resolution from 20,000 m to 70 m, 1.6 million nodes.

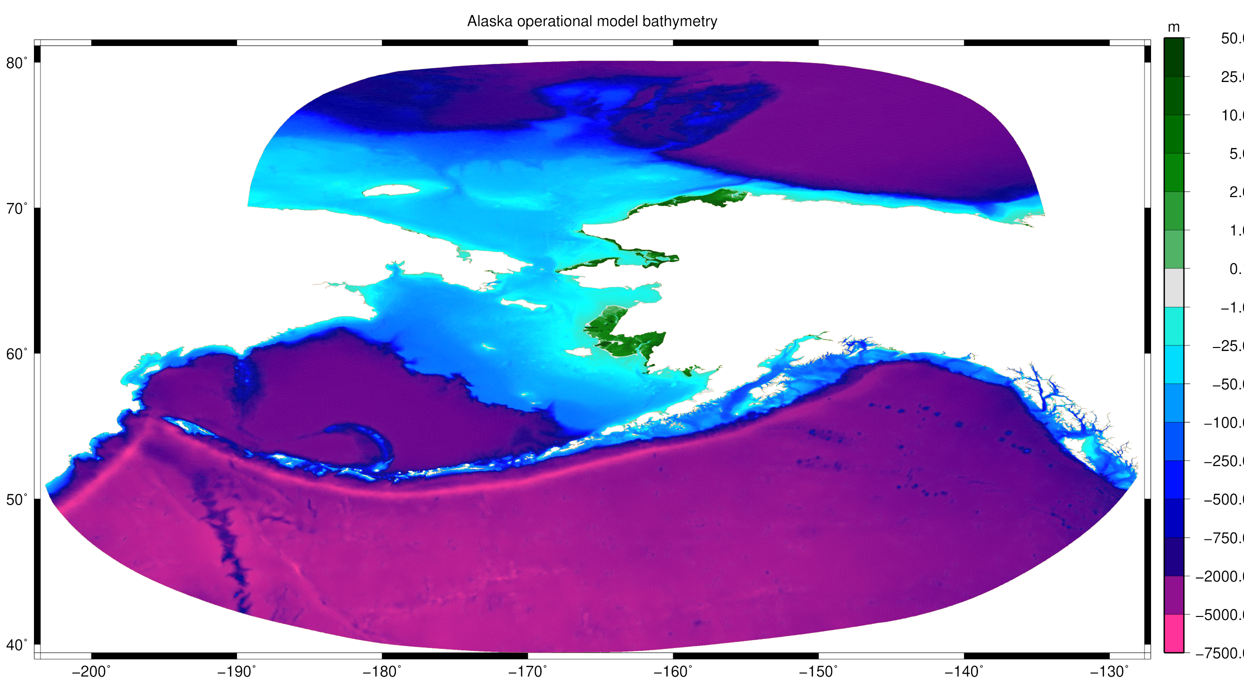

FIG. 3: Model bathymetry

unstructured mesh of the model domain was generated by using a script-based mesh generator called OceanMesh2D (Roberts et al. 2019a). The mesh generation is carried in two steps: the mesh of the open water side is first created; subsequently, the mesh on the land side is generated with nodes string of relevant portions of outer boundary extracted from the mesh of the ocean side as it boundary. The final mesh is simply a union of these two meshes. By building mesh in this manner, the boundary between land and water are distinctively delineated, i.e. the computational grid conforms to the coastlines. The OceanMesh2D parameters for the ocean side of the mesh were set to: minimum element size MinEle=1,000 m; maximum element size MaxEle=20,000 m; wavelength to mesh size ratio WL=300; target time step DT=2s; max allowable triangle-to-triangle transition rate in the mesh g=0.2; number of elements to resolve feature width R=2; a non-dimensional number directly proportional to the number of triangles per bathymetric slope and inversely proportional to the bathymetric depth SLP=20; the decimal percent the edge length changes in space DIS=0.35; max resolution near shore MaxEle-ns=1,000 m. Bounding boxes are defined for various coastal regions where more detail is desired including Cook Inlet, Bristol Bay, the Aleutian Islands, Kotzebue Sound, and St. Lawrence Island where we set MinEle=200 m. For the floodplain side, there are two floodplains in the mesh, the first one is located in the north of Alaska, the second one is at Yukon Delta: for floodplains along the Arctic MinEle=200 m, and for the Yukon Delta floodplain we set MinEle=100 m.

Fig. 2 shows a comparison of the mesh resolution of the previous generation high resolution mesh (Joyce et al. 2019) and the present operational model. As shown in the figures, the high resolution mesh (Fig. 2(a)), which contains 4.1 million nodes, has similar high resolution in the north Pacific Ocean and Bering Sea and higher resolution of up to 25m along the coastal areas of western Alaska. Meanwhile, the present operational mesh (Fig. 2(b)) has only 1.6 million nodes with targeted high resolution in and around steep topographic features in the deep ocean and along shelf breaks and with higher resolution for near coastal waters and floodplains. By using the lighter present model, the wallclock time for a five day forecast is about 1 hour using 240 cores on our parallel cluster (Lenovo NeXtScale nx350M5, 83 Dual Intel Xeon E5-2680 v3, clock rate 2.50GHz, FDR 56 GB Infiniband, 5,120 GB total RAM), compared to the high resolution model which takes about 8 hours, the present model is much more efficient for forecasting purposes.

The bathymetry applied to the present operational model is shown in Fig. 3. For bathymetric data sources, we use the GEBCO2020 bathymetry (15 arc-second grid of 43,200 rows × 86,400 columns) as a background bathymetry, then blend in the Smooth Sheet bathymetries of Aleutian Islands (100 m resolution, Zimmermann et al. (2013)), Cook Inlet (50 m resolution, Zimmermann and Prescott (2014)), Central Gulf of Alaska (100 m resolution, Zimmermann and Prescott (2015)), Norton

Sound (100 m resolution, Prescott and Zimmermann (2015)), and the Southern Alaska Coastal Relief Model (CRM, 24 arc-second resolution, Lim et al. (2011)) bathymetry to the Inside Passage area, the Bristol Bay and the Yukon River area. Moreover, for the Kuskokwim River, we apply the NOAA chart bathymetry (US4AK85M). We note that there are many regions where high quality bathymetry is simply not available and that we applied the best available databases.

For the internal tidal dissipation, a scalar model was applied with $C_{it} = 1.2$ and we limited internal tide dissipation to depths equal to or greater than 100 m. For the bottom friction, we are using a global $C_f = 0.0015$, and local C_f values for the Cook Inlet 0.003, Bristol Bay 0.0012, Kotzebue Sound 0.005, Akutan Bay 0.001, Tigalda Bay 0.003, Teller Port 0.0025.

f. Forecasting method of ALCOFS

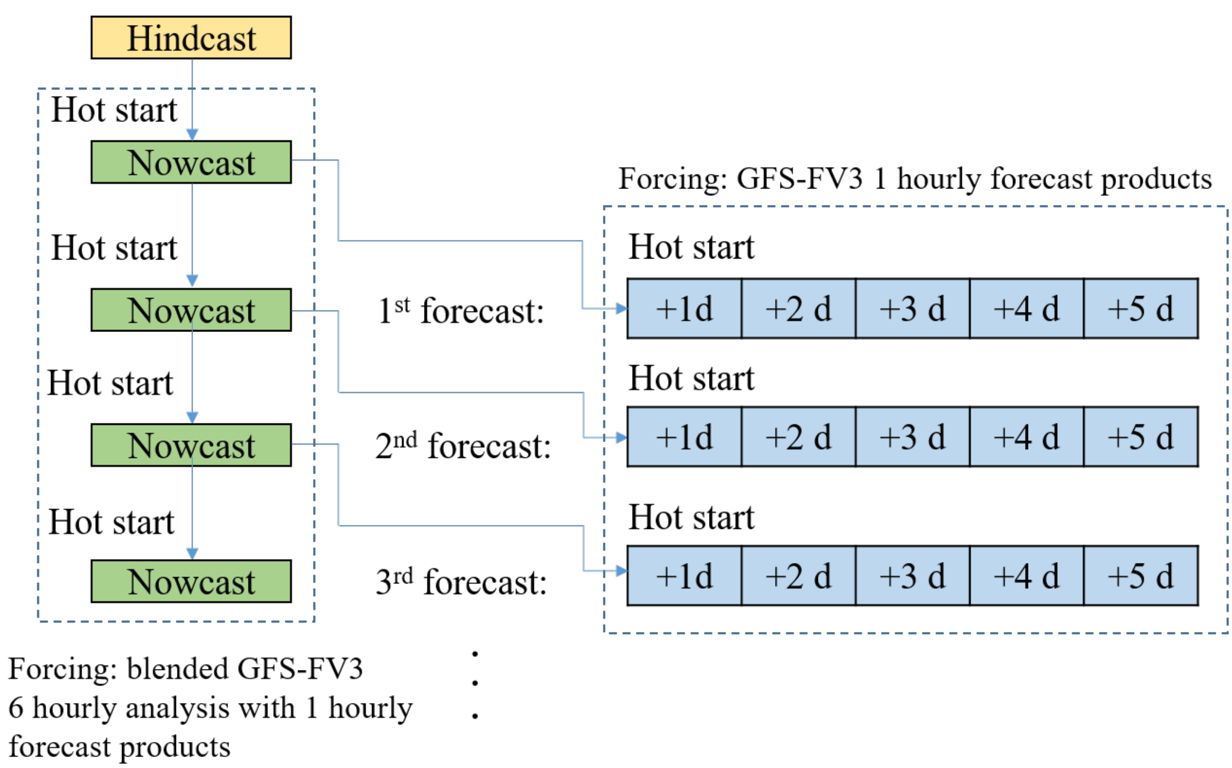

FIG. 4: A real-time forecasting flowchart for storm surge.

Fig. 4 shows the forecasting flowchart of the Alaska Coastal Ocean Forecast System (ALCOFS). First, the system starts with a hindcast to spin-up the system, in this study, we do a 12 day hindcast with 5 day spin-up which turns out to work well. Regarding to the forcing data for the 12 day

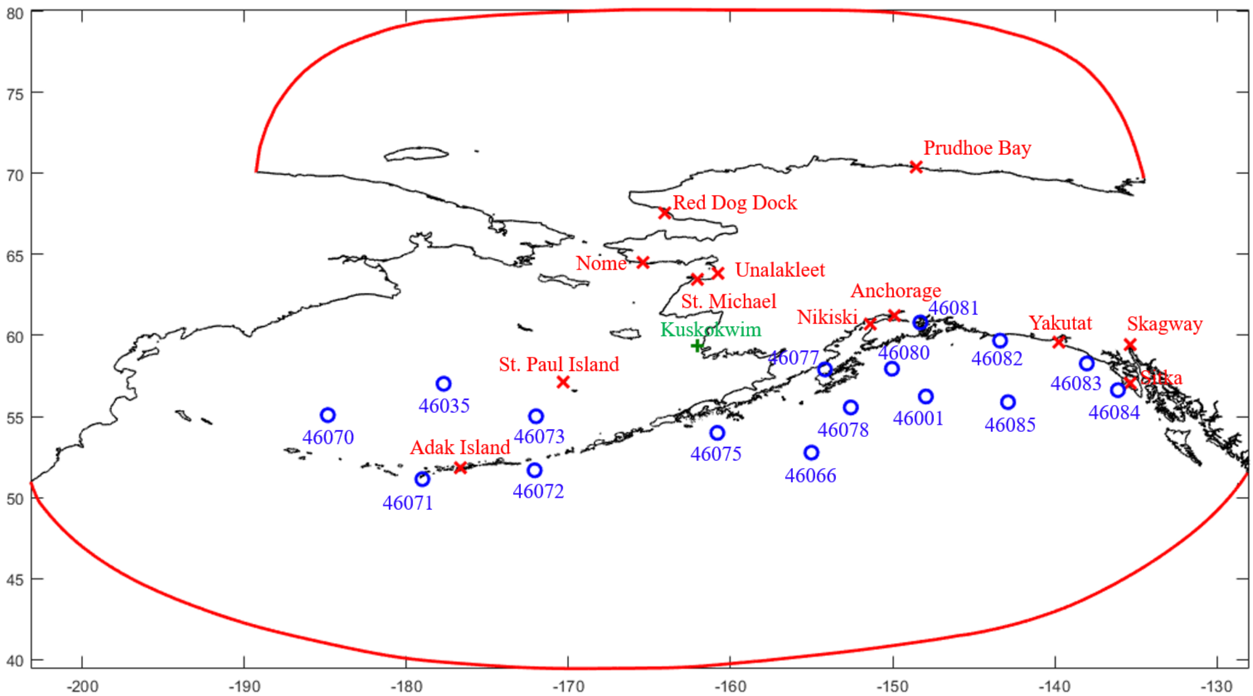

FIG. 5: Recording stations and buoys

hindcast, we notice that there is a gap between the hindcast and forecast forcing products (GFS-FV3) for the current date. Therefore, we run 10 day hindcast with 3 hourly GFS-FV3 hindcast products (wind, pressure, ice), then run another 2 days using 6 hourly analysis and 1 hourly forecast blended GFS-FV3 products (at the time we started the system, there was a 3 day gap, so for the following nowcast days also use the same blended products), in this way, we can use as much as possible reanalysis data. Second, the present system runs a 6 day nowcast/forecast simulation (1 day nowcast, 5 day forecast, hot started at the end of the previous nowcast simulation, followed by the updated one day nowcast and followed by the most up to date 5 day forecast) for each cycle. 1 hourly GFS-FV3 forecast products (0.25 degree resolution) are applied in the forecast periods. Fig. 5 shows the water level stations (red cross marks) and buoys (blue circle marks) for wave that we are recording the model results, so that we can provide live comparison to the observational data and the latest 5 day forecast results at these places.

3. Tidal validation

For the storm surge forecasting, it is essential to get the tidal signals correct, so the parameters of internal tide coefficient (C_{it}) and the bottom friction coefficient (C_f) have been optimized by

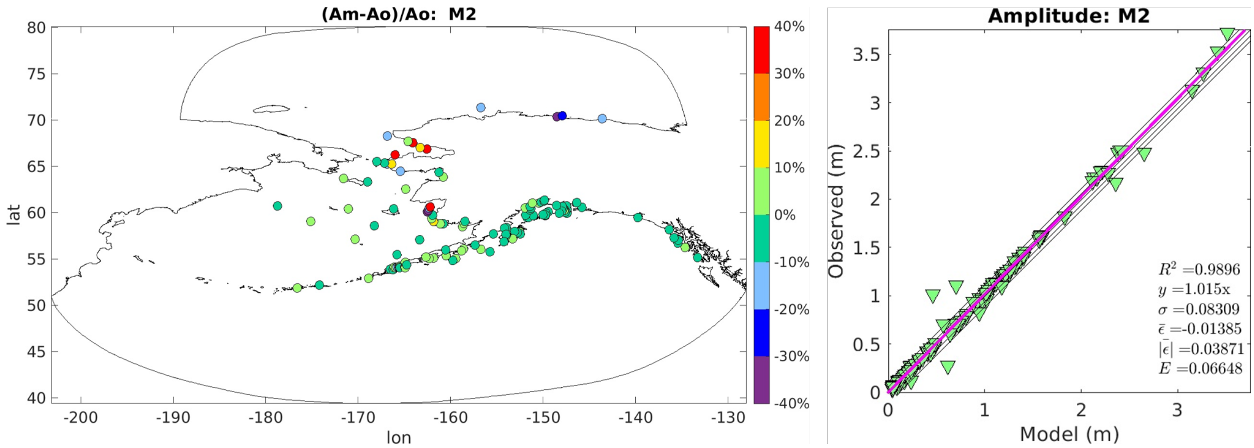

FIG. 6: M2 amplitude performance

validating with the observational data. For the tidal validation, we did a tidal simulation test for the period from July 14, 2020 to September 19, 2020 (total 68 days with 18 day spin up) and harmonically analyzed the resulting history records over the last 50 days. Eight dominant astronomical tidal harmonic constituents (M_2, N_2, S_2, K_2, K_1, Q_1, O_1, P_1) are forced on the open ocean boundaries. The boundary forcing was extracted from the TPXO9-atlas-v1/v4 data assimilated global tidal solutions. In addition, the same eight constituents are forced using the tidal potential functions as well as the self attraction and load tides are forced at each node within the model domain. The setups of ADCIRC are as follows, ICS=-22 (Mercator projection with pole rotation), IM=511113 (implicit mode), A00=0.4, B00=0.4, C00=0.2 (time weighting factors), H0=0.1 (minimum water depth), TAU0=-3 (Generalized Wave-Continuity Equation weighting factor that weights the relative contribution of the primitive and wave portions of the GWCE), NTIP=2 (tidal potential and self attraction / load tide forcings are used), DT=20 s (simulation time step). The simulation results of the present model are compared to the same 121 gauges used in Joyce et al. (2019).

A comparison of M_2 amplitudes between the observation data and model results is shown in Fig. 6. Overall, most of the stations are under 5 percent error, except a few stations in the Kuskokwim River, Kotzebue Sound and Prudhoe Bay. We note that these stations with relatively high percentage errors lie within the Kuskokwim River where the bathymetric data are clearly not realistic and are not consistent between the various databases, specifically GEBCO2020, CRM, and the NOAA charts. The higher errors associated with regions north of the Bering Strait including the

		M_2 A.	N_2 A.	K_1 A.	O_1 A.	M_2 P.	N_2 P.	K_1 P.	O_1 P.	All A.	All P.
R^2	FES2012	0.955	0.867	0.813	0.933	0.893	0.890	0.918	**0.936**	0.966	0.875
	TPXO9-atlas-v1	0.887	0.750	0.882	0.901	0.915	0.898	0.910	0.882	0.921	0.862
	TPXO9-atlas-v4	0.974	0.942	**0.947**	**0.971**	0.931	0.930	**0.945**	0.920	0.985	0.910
	Joyce et al. (2019)	0.962	0.947	0.899	0.845	**0.956**	**0.953**	0.921	0.902	0.976	0.907
	Operation(tpxo9v1)	**0.990**	0.974	0.914	0.918	0.952	0.945	0.915	0.933	**0.989**	**0.913**
	Operation(tpxo9v4)	0.988	**0.975**	0.917	0.924	0.938	0.941	0.905	0.926	**0.989**	0.906
σ	FES2012	0.196	0.059	0.084	0.032	38.585	38.215	25.295	22.925	0.087	39.552
	TPXO9-atlas-v1	0.335	0.102	0.070	0.039	34.566	37.452	34.312	28.912	0.137	42.003
	TPXO9-atlas-v4	0.130	0.038	**0.045**	**0.021**	29.297	30.227	**21.582**	26.159	0.052	33.199
	Joyce et al. (2019)	0.157	0.036	0.061	0.048	**23.904**	**22.874**	33.776	27.748	0.065	33.707
	Operation(tpxo9v1)	**0.083**	**0.028**	0.061	0.038	24.709	25.458	26.562	**21.396**	**0.044**	**32.194**
	Operation(tpxo9v4)	0.089	**0.028**	0.059	0.037	28.316	26.362	28.173	23.434	0.045	33.568
$\bar{\epsilon}$	FES2012	-0.076	-0.006	-0.022	-0.011	-4.654	-3.076	**0.713**	-4.291	-0.019	-3.988
	TPXO9-atlas-v1	0.033	0.013	-0.005	-0.010	-3.407	**-1.628**	4.118	-3.188	0.005	-2.651
	TPXO9-atlas-v4	**0.012**	**0.001**	**-0.004**	**-0.004**	**0.132**	-4.713	-2.778	-7.431	**-0.001**	-3.091
	Joyce et al. (2019)	-0.015	-0.004	**-0.004**	-0.013	2.422	3.609	9.759	-5.908	-0.006	**0.658**
	Operation(tpxo9v1)	-0.014	-0.012	0.016	0.010	-1.939	3.427	5.115	**-1.822**	-0.002	0.936
	Operation(tpxo9v4)	-0.009	-0.012	0.017	0.010	1.176	1.837	3.499	-4.030	-0.002	0.855
$\lvert\bar{\epsilon}\rvert$	FES2012	0.127	0.033	0.048	0.019	17.965	19.267	12.071	11.208	0.038	20.499
	TPXO9-atlas-v1	0.155	0.049	0.034	0.019	17.033	19.780	15.640	14.712	0.044	21.428
	TPXO9-atlas-v4	0.051	**0.017**	**0.023**	**0.012**	11.338	13.091	**7.476**	10.934	**0.017**	**14.671**
	Joyce et al. (2019)	0.080	0.019	0.034	0.024	11.309	**10.957**	16.099	12.374	0.026	16.571
	Operation(tpxo9v1)	**0.039**	0.018	0.035	0.021	**10.660**	11.505	12.156	**9.791**	0.021	15.742
	Operation(tpxo9v4)	0.046	0.018	0.035	0.020	13.077	11.625	13.024	11.380	0.021	16.582
E	FES2012	0.166	0.223	0.193	0.117	0.157	0.163	0.096	0.093	0.171	0.157
	TPXO9-atlas-v1	0.266	0.388	0.155	0.139	0.141	0.161	0.134	0.116	0.265	0.166
	TPXO9-atlas-v4	0.103	0.144	**0.099**	**0.074**	0.116	0.128	**0.083**	0.108	0.101	0.131
	Joyce et al. (2019)	0.125	0.137	0.137	0.173	**0.096**	**0.097**	0.136	0.104	0.127	0.132
	Operation(tpxo9v1)	**0.066**	**0.115**	0.140	0.135	0.098	0.108	0.104	**0.085**	**0.086**	**0.127**
	Operation(tpxo9v4)	0.071	**0.115**	0.137	0.132	0.112	0.111	0.109	0.095	0.088	0.132

TABLE 1: Measured and analyzed difference statistics (R^2, standard deviation σ, average error $\bar{\epsilon}$, absolute average error $|\bar{\epsilon}|$, and normalized root-mean-square error E), the FES2012 results are from Joyce et al. (2019) compared to 121 stations.

stations at Kotzebue Sound and Prudhoe Bay may be associated with inaccuracies of the boundary tidal forcing across the Arctic Ocean. Preliminary studies of the global model suggest that more accurate results are associated with the elimination of all the boundary forcings. We also note that there are strong SSA and SA constituents in the Arctic associated with high freshwater summer inflows and the Beaufort Gyre.

Table 1 summarizes the error statistics for the FES2012 global tidal model, the high resolution model of Joyce et al. (2019), TPXO9-atlas-v1, TPXO9-atlas-v4 (released on Dec. 24, 2020, Egbert and Erofeeva (2002)), and the present operational model. Overall, the results of the present model are very good with R^2 values for the semi-diurnal M_2 amplitude of 0.990 and 0.988 for v1 and v4 respectively and ranging between 0.975 and 0.905 for the other 7 primary constituents. The absolute average error of M_2 amplitude for the present model is the smallest at 3.9 cm. The normalized root-mean-square error (E) is also the smallest for all the 8 constituents of the present model. The error statistics for the operational model are clearly consistently better than the other models. And the operational model forced by the TPXO9-atlas-v1 seems to be slightly better than the TPXO9-atlas-v4, but very close to each other. For the following simulation, we adopt the TPXO9-atlas-v1 as the open boundary forcing.

4. Sea ice effect to storm surge

In order to evaluate the impact and effectiveness of the sea ice to storm surge, four large winter storm events with different sea ice conditions and coverage were simulated. Fig. 7 shows the sea ice coverage images during the four storm events in February 2011, November 2011, January 2017 and February 2019. Fig. 8 shows the effects of sea ice on maximum modeled water level (with ice minus without ice) for the four storms. February 2011 shows the greatest sea ice extent across the Bering Shelf, and results in an increase in water level 10-30 cm across a large area of Bering Strait due to the air-sea momentum transfer under ice coverage. November 2011 shows less sea ice coverage in the Bering Strait which results in less ice effect on the maximum water level changes but still adding around 10 cm across Norton Sound. January 2017 and February 2019 storms show high percentage of sea ice coverage over the Norton Sound which both result in a large impact to the water level in that area, a 30 to 50 cm lift across the Norton Sound. Fig. 9 show the sea ice concentrations, water level validations and differences of water levels between without (w/o) ice and with (w/) ice cases for the Nome station. From Fig. 9, we can see w/ ice case turns out to match the observations better than the w/o ice case especially during the storm peaks, Feb. 18/25, 2011, Nov. 10, 2011, Jan. 1, 2017, Feb. 13, 2019. We also notice that by considering the ice effects, the water level could increase 10 to 30 cm during the storms at Nome station. Tables 2 and 3 show the statistics of w/o and w/ ice models for the four storms at the Nome and Red Dog Dock stations.

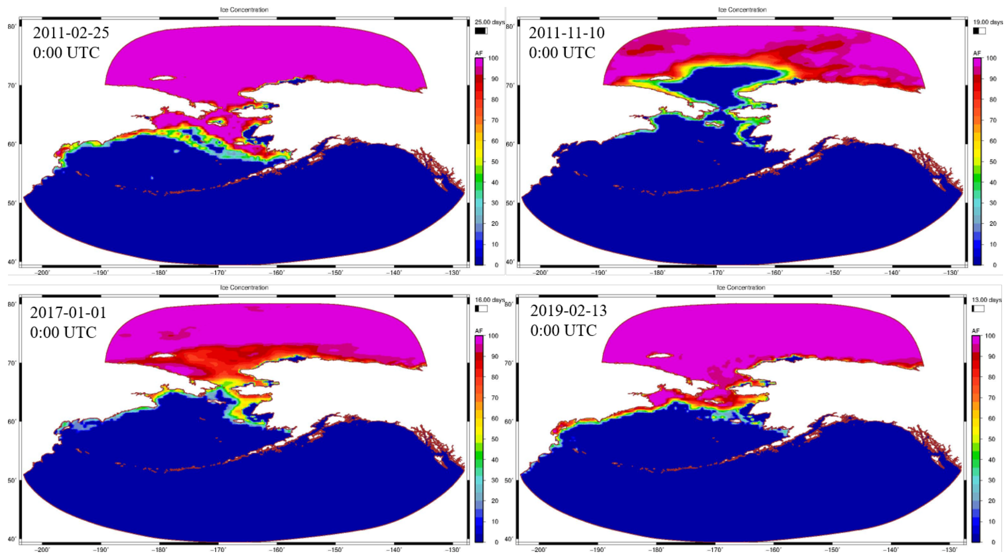

FIG. 7: Ice concentrations for 4 different storms.

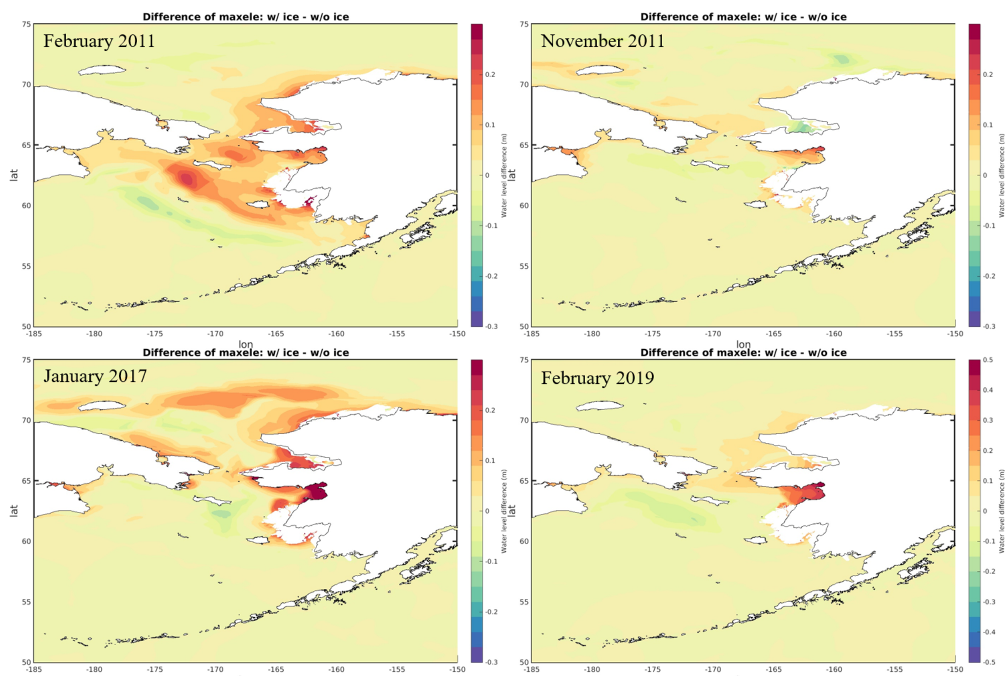

FIG. 8: Effect of sea ice on maximum modeled water level (with ice minus without ice) for February 2011, November 2011, January 2017 and February 2019.

In the tables, Peak indicates the maximum water level during the simulation periods, RE is the relative error of the maximum values between observations and simulations, R^2 is the coefficient of determination, $\bar{\epsilon}$ is the average difference, $|\bar{\epsilon}|$ is the averaged absolute difference, NRMSE is normalized root mean square error, σ is the standard deviation and WSS is the Willmott skill score

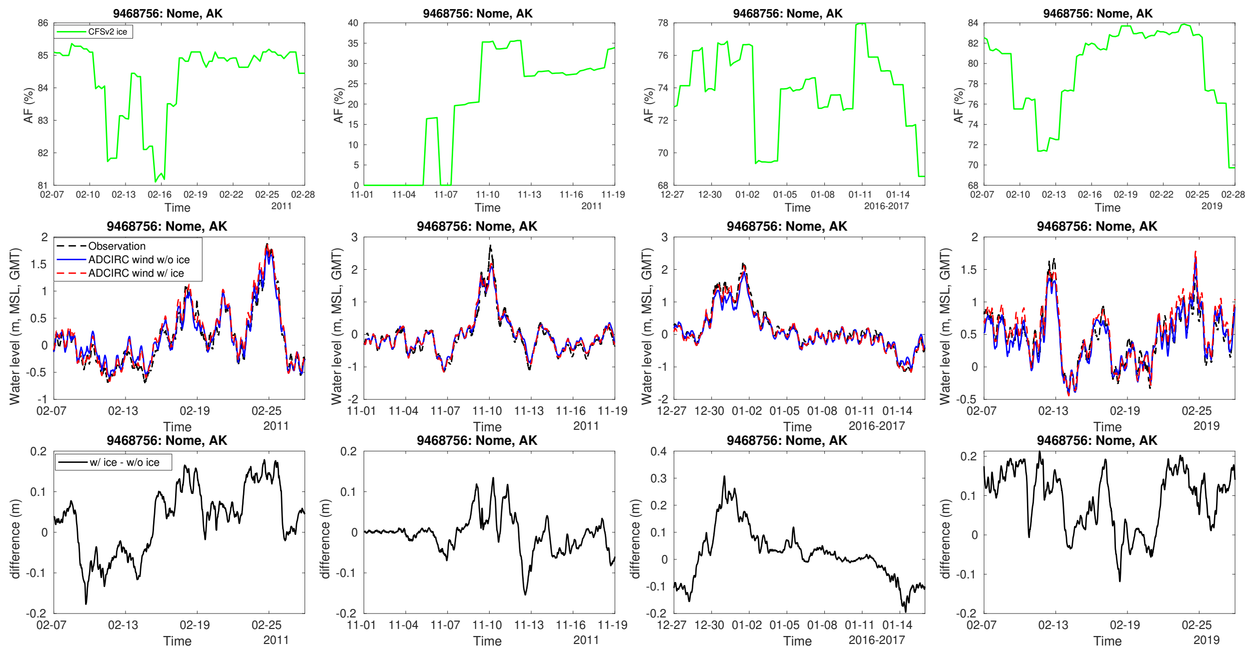

FIG. 9: Sea ice concentrations, water level validations and water level differences at Nome station for different storms.

(1 for perfect match between observation and simulation and 0 for no agreement) (Willmott 1981). We can see that generally the error statistics improved for the with ice model as compared to the without ice model. Compared with the w/o ice cases, the RE of the w/ ice cases reduced maximum 8.04% (Jan. 2017 from -12.40% to -4.36%) at Nome and maximum 11.28 % (Jan. 2017 from -27.72% to -16.44%) at Red Dog Dock. For the Nome station, the R^2 are above 0.91, the $\bar{\epsilon}$ are less than 8 cm, the $|\bar{\epsilon}|$ are less than 11cm, the NRMSE are less than 0.25, the σ are less than 0.13 and the WSS are above 0.97. For the Red Dog Dock station, the R^2 are above 0.8, the $\bar{\epsilon}$ are less than 8 cm, the $|\bar{\epsilon}|$ are less than 17cm, the NRMSE are less than 0.45, the σ are less than 0.17 and the WSS are above 0.94. The statistics for the without ice model as compared to the with ice model demonstrates that the added physics improves the solution as compared to the station data.

5. Wave effect to storm surge

In this section, the wave model performance and its effect to storm surge are evaluated. The same four storms as the previous section are simulated by using the SWAN+ADCIRC model with sea ice forcing. Figs 10 show the validations of wind speeds, wind directions and significant wave heights at the NDBC buoys with available observational data for the Nov. 2011. In general, for

	Peak	RE	R^2	$\bar{\epsilon}$	$\lvert\bar{\epsilon}\rvert$	NRMSE	σ	WSS
obs. (Feb. 2011)	1.8810							
w/o ice	1.7370	-7.66%	0.9468	0.0463	0.1131	0.2479	0.1312	0.9824
w/ ice	1.8698	-0.59%	0.9603	0.0794	0.1098	0.2441	0.1116	0.9847
w/ ice&wave	1.8840	0.16%	0.9600	0.0849	0.1131	0.2508	0.1122	0.9839
obs. (Nov. 2011)	2.7560							
w/o ice	2.0944	-24.01%	0.9657	0.0322	0.0891	0.2127	0.1198	0.9873
w/ ice	2.1826	-20.81%	0.9666	0.0287	0.0804	0.1947	0.1098	0.9898
w/ ice&wave	2.2250	-19.27%	0.9657	0.0527	0.0901	0.2102	0.1107	0.9882
obs. (Jan. 2017)	2.2050							
w/o ice	1.9315	-12.40%	0.9686	-0.0519	0.1082	0.2249	0.1325	0.9840
w/ ice	2.1088	-4.36%	0.9758	-0.0437	0.0835	0.1650	0.0948	0.9924
w/ ice&wave	2.1735	-1.43%	0.9759	-0.0269	0.0787	0.1552	0.0945	0.9934
obs. (Feb. 2019)	1.6710							
w/o ice	1.3663	-18.23%	0.9142	-0.0485	0.1056	0.2151	0.1218	0.9719
w/ ice	1.4909	-10.78%	0.9155	0.0399	0.1036	0.2154	0.1251	0.9753
w/ ice&wave	1.5164	-9.25%	0.9141	0.0541	0.1074	0.2252	0.1261	0.9730

TABLE 2: Comparisons of water levels (m) between the observations and model simulations for 4 storms at Nome station.

	Peak	RE	R^2	$\bar{\epsilon}$	$\lvert\bar{\epsilon}\rvert$	NRMSE	σ	WSS
obs. (Feb. 2011)	2.106							
w/o ice	1.7861	-15.19%	0.9387	-0.0134	0.0971	0.2387	0.1217	0.9826
w/ ice	1.9204	-8.81%	0.9376	0.022	0.0999	0.2454	0.1239	0.9833
w/ ice&wave	1.9294	-8.38%	0.9373	0.0256	0.1006	0.2474	0.1243	0.983
obs. (Nov. 2011)	1.503							
w/o ice	1.1847	-21.17%	0.834	-0.0571	0.1246	0.4338	0.1533	0.947
w/ ice	1.1896	-20.85%	0.8346	-0.0723	0.1333	0.4551	0.1556	0.9463
w/ ice&wave	1.202	-20.03%	0.8295	-0.0559	0.1262	0.4435	0.1576	0.9483
obs. (Jan. 2017)	1.928							
w/o ice	1.3935	-27.72%	0.9042	-0.1113	0.1639	0.3578	0.1619	0.962
w/ ice	1.6111	-16.44%	0.9077	-0.1041	0.1681	0.3633	0.1701	0.9657
w/ ice&wave	1.6292	-15.50%	0.907	-0.0944	0.1655	0.3566	0.1716	0.967
obs. (Feb. 2019)	1.125							
w/o ice	0.8951	-20.44%	0.7984	-0.0708	0.1284	0.3615	0.1427	0.9263
w/ ice	0.9329	-17.08%	0.8236	-0.0307	0.1138	0.3183	0.1369	0.9498
w/ ice&wave	0.9511	-15.46%	0.8257	-0.0214	0.1111	0.3121	0.1358	0.9516

TABLE 3: Comparisons of water levels (m) between the observations and model simulations for 4 storms at Red Dog Dock station.

most of the buoys the forcing data and the model results match the observations pretty well, except the buoy 46081 at Western Prince William Sound, where the forcing wind products are not well matching the observations which results in the pool performance of the model results. Similarly the buoy 46077 at Shelikof Strait, the wind products also relative under predicted and we can see the the model results didn't capture the peaks well. Fig. 11 shows the effects of wave on maximum modeled water level (with wave minus without wave) for the four storms. The impacts from waves to the water level show non-negligible effects (30 cm increased during the November 2011 storm when there was the fewest sea ice coverage compared to the other storms) for the nearshore area at the Yukon Delta. In order to see the waves effects to at the station, Fig. 12 show the significant wave heights, water levels compared to observations and the water level differences between the SWAN+ADCIRC model and ADCIRC model at the Nome station for four different storms. As showed in Fig. 7, Nov. 2011 shows the fewest ice coverage in the Kotzebue Sound, Bering Straight, and Norton Sound, and it is the largest storm among the four storms, the model results show relatively high significant wave height at the stations, 3.5 m at Nome. And we can also see the waves effects add maximum 8 cm to the water level at the Nome station. From the Tables 2 and 3, we can also see by adding the wave physics reduced the RE at both the Nome and Red Dog Dock stations. For the other statistics, the one w/ ice&wave are very close to the one w/ ice.

6. Investigations of long term storm surge hindcast

In order to better understand the seasonal sea level trends, we implemented a continuous 3 year long term hindcast, started from September 1, 2016 to the end of September, 2019 (total 1,125 days, with 30 day spin-up). This run was forced with CFSv2 (Saha and Coauthors 2014) atmospheric and ice products (1 hourly wind, pressure, and 6 hourly ice concentration). And for the tidal forcing, twelve constituents were included: the semi-diurnal M_2, N_2, S_2, K_2; the diurnal K_1, Q_1, O_1, P_1; and the long-period S_A (solar annual), S_{SA} (solar semiannual), M_M (lunar monthly), M_F (lunar fortnightly). The tidal potential and the self attraction and load tide are forced at each node within the model domain, and eight dominant astronomical tidal constituents (M_2, N_2, S_2, K_2, K_1, Q_1, O_1, P_1) are forced on the north and south open ocean boundaries. The boundary forcing was extracted from the TPXO9-atlas-v1 data assimilated global tidal solutions.

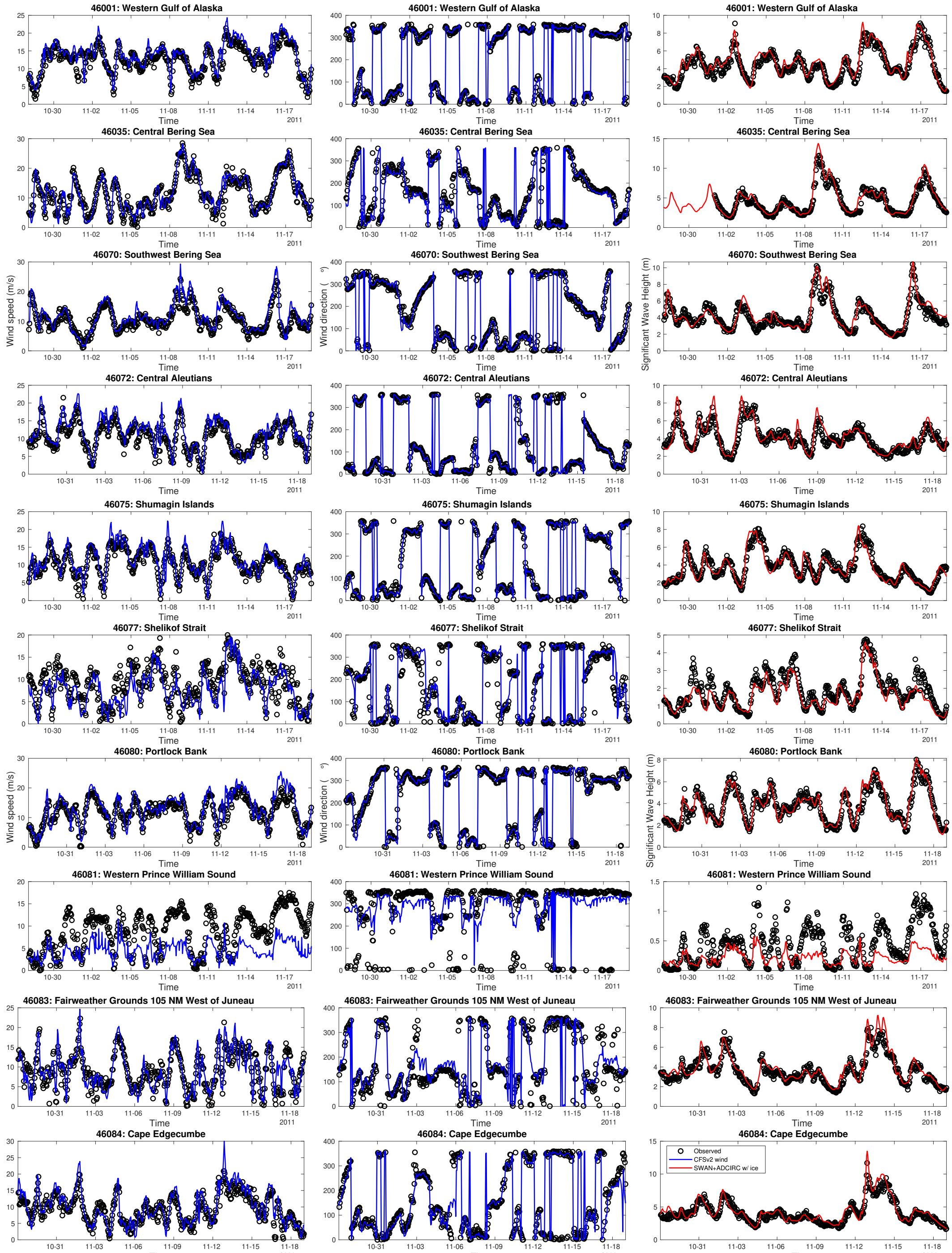

FIG. 10: Validations of wind speeds (left), wind directions (middle) and significant wave heights (right) for the Nov. 2011 storm.

Fig. 13 shows the water level comparisons at four stations for the whole simulation time period. By looking at the time series comparisons, we can see the model results are in good agreement

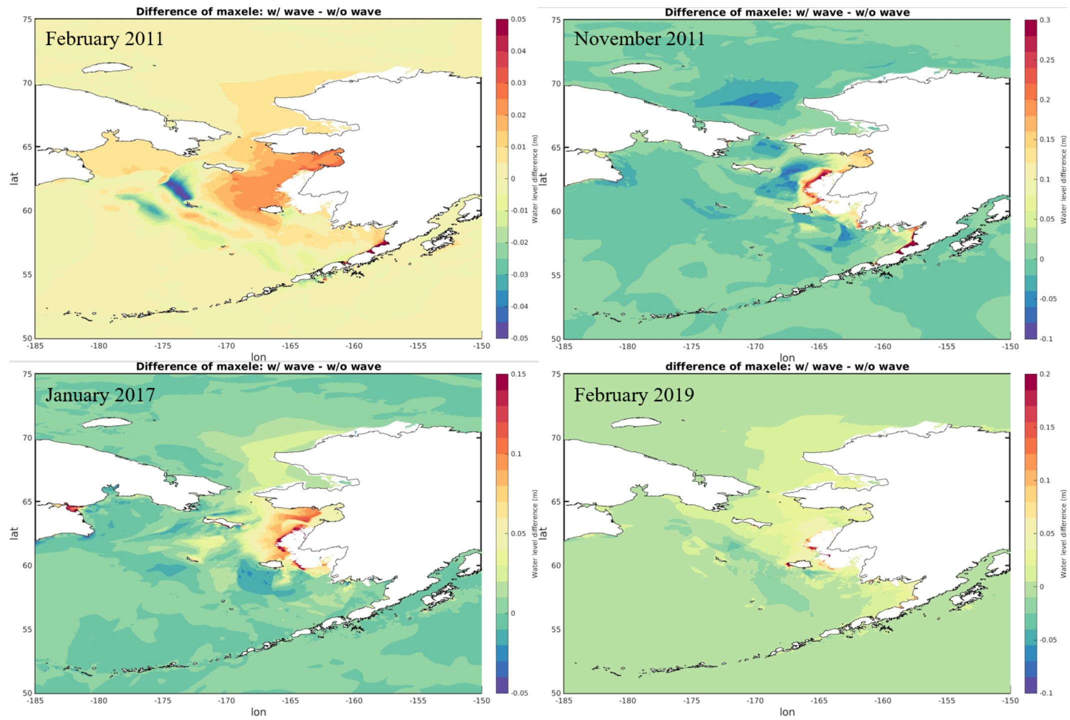

FIG. 11: Effect of wave on maximum modeled water level (with wave minus without wave) for February 2011, November 2011, January 2017 and February 2019.

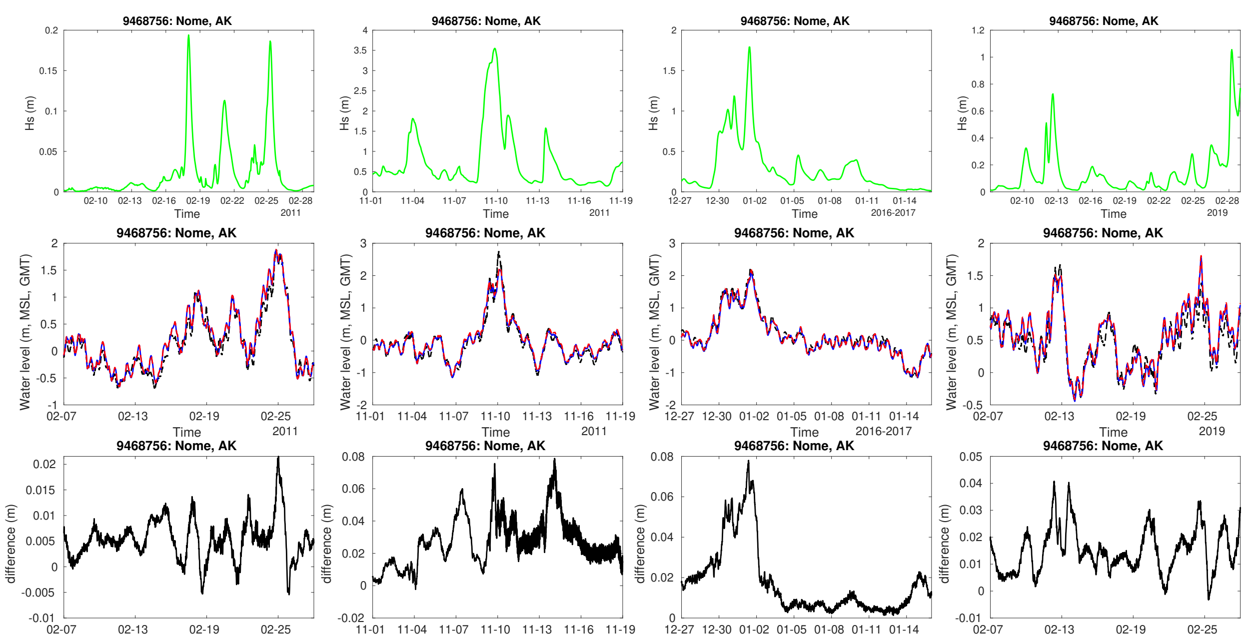

FIG. 12: Significant wave height, water level validations and differences at Nome station for 4 different storms.

with the observational data, except the model could not capture the troughs below -0.5 m at the Prudhoe Bay station, this is due to the limitation of the bathymetry in the model at the location is 0.5 m due to aliasing of the bathymetric data. From the scatter plots, we can see the coefficient of determination (R^2) are above 0.8 except Prudhoe Bay, and for the averaged absolute difference ($|\bar{\epsilon}|$), Nome is 8 cm, Red Dog Dock and Prudhoe Bay are 10 cm, but Unalakleet is relatively high 20 cm which is because the observational data is not reliable at this station throughout the year and especially during the ice season due to entrance siltation as well as ice blockages. We note that NOAA's Tides and Currents web data portal states that "Significant changes in the tidal range at this location are due to interactions with the shoals and sandbars at the entrance to the Unalakleet River. The water level data and datums are only representative of the oceanographic conditions upstream of the entrance." The problem is related to the fact that this station is embedded into the inlet system which has a very narrow entrance and is routinely blocked by silting and/or ice, neither of which are included in the model. We do note that the high tide is generally well matched, while the low tide is not since the station measurements rarely drop below mean sea level due to the silt and/or ice blockages.

In order to validate the frequency content of the sea surface variations, the power spectral density is computed through the MATLAB function *pmtm* employed Thomson's multitaper power specral density method (Thomson 1982). Fig. 14 shows a comparison of the power spectral densities of the 6-minute sea level variations for both our long term simulation and the station measured signal over the same three year period at eleven different stations. From the figure, we can see levels of the spectral density spectrum are well represented by the presented model, and the comparisons show the model results in the sub-tidal and tidal range between the M_F and M_4 tides are in good agreement with observations. For the longer frequencies in the vicinity of the semiannual (S_{SA}) frequency, the model results at Nome, Red Dog Dock, Unalakleet, and Adak Island are in good agreement with observations but at the other stations including Prudhoe Bay in the Beaufort Sea, St. Paul Island in the Bering Sea, and Anchorage and Nikiski in Cook Inlet, and Skagway, Yakutat Bay and Sitka along the Gulf of Alaska are underestimated. The long period S_{SA} and S_A are small compared to the other tidal constituents and they are driven primarily by the seasonal changes in wind, water temperature, atmospheric pressure, salinity and current systems that affect water level (Parker 2007). While our model does fully incorporate atmospheric wind and pressure, it does not yet consider temperature and salinity effects and/or the associated baroclinically driven current systems which will be incorporated in a future upgrade. These effects will reflect seasonally varying fresh water discharges, vertical density structures, and ocean current systems. For the super tidal frequencies, half of the stations show differences between model and observation above 20 to 50 cycles per day, i.e. below periods of one hour to 15 minutes. The poorly performing higher frequency stations include Nome, Red Dog Dock, St Paul Island, Adak Island, and Yukutat Bay. We speculate that reason for the poorer fit might be from the instrument noise where the spectrum is relatively flat in the observations (Savage et al. 2017; Pringle et al. 2019), or due to the limitation from the forcing data (one hourly winds, atmospheric pressures and 6 hourly sea ice). Alternatively there may be features in the hydrodynamic response, such as eddies being shed locally, that are not yet being resolved. This will be a target of future investigations as we further resolve the coasts.

To further analyze the three year simulation, we have derived from the preliminary long-term signal at targeted stations for 36 months (10-01-2016 through 9-30-2019): 1. The raw difference between observations and model results. 2. The moving average for 30 day window of the raw difference. Ten analyzed station results are presented in Figs. 15. We note that there appears to be a summer high that is missed in the Arctic, likely associated with fresh water from river and land margin discharges and/or possibly associated with the Beaufort Gyre (one of the two major ocean currents in the Arctic Ocean). All stations appear to be performing poorly in a roughly fortnightly oscillation.

7. Validation of the one year nowcast and forecast results

In this section, the nowcast and forecast results of water levels, significant wave heights and forcing products are validated by comparing to the observational data from NOAA stations and NDBC buoys for the operational period from September 10, 2020 to September 10, 2021. In the ALCOFS, we are running three operational models, one is SWAN+ADCIRC, and the other two are wave models using WWIII (regional Alaska model and global model) to see the effectiveness compared to the SWAN model. For the setups of each model, in the ADCIRC, we are using explicit mode, $\Delta t = 2$ s, 1 hourly foring wind, atmospheric pressure, sea ice concentration, eight dominant astronomical tidal constituents (M_2, N_2, S_2, K_2, K_1, Q_1, O_1, P_1) are forced on the north and south

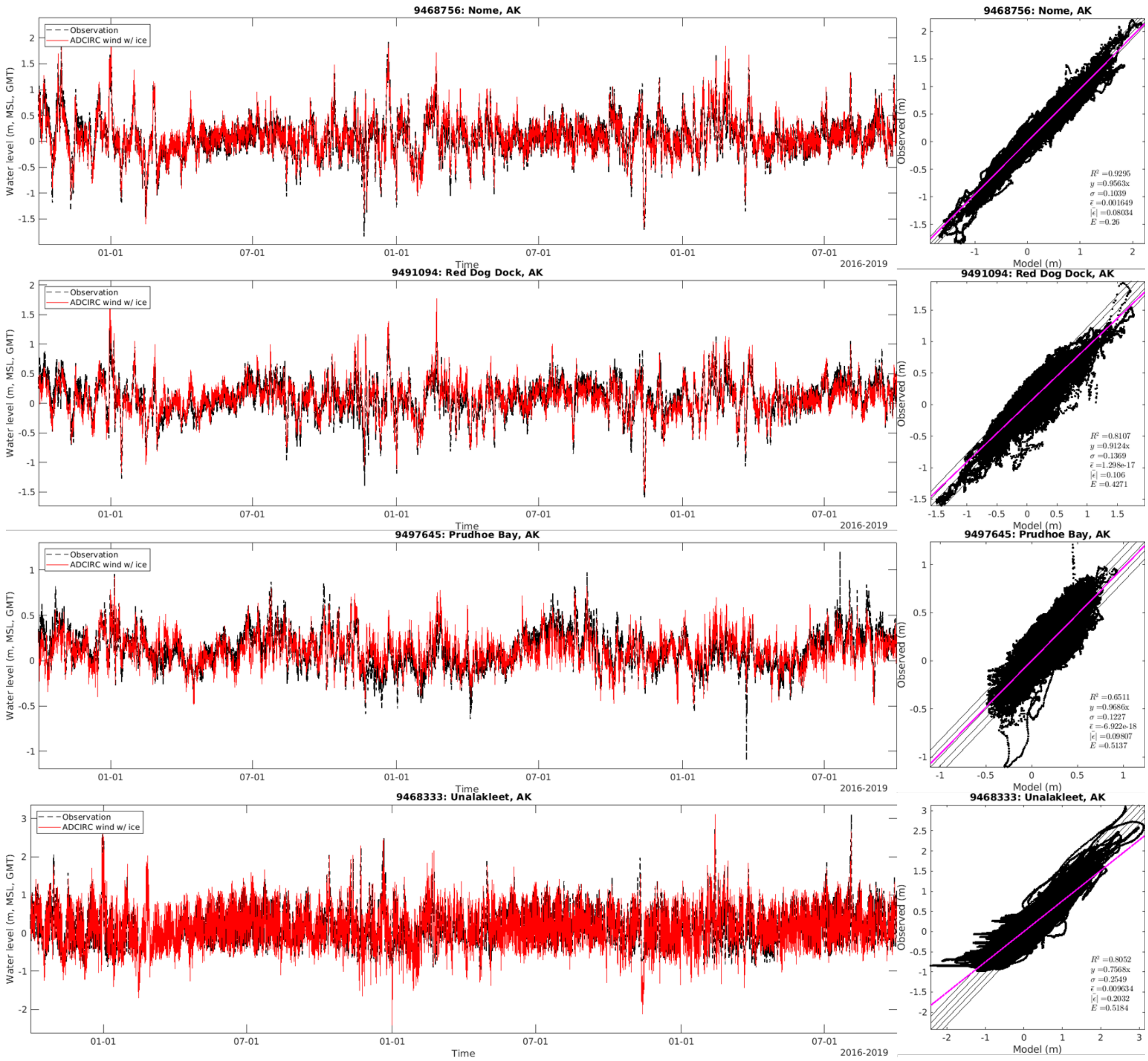

FIG. 13: Validation of water level.

open ocean boundaries, and the same constituents of tidal potential and self attraction and load tide are forced for all the nodes. In the SWAN model, we are using $\Delta t = 3600$ s, the frequencies range from 0.035 to 0.9635 Hz and are discretized into 40 bins on a logarithmic scale. The wave directions are discretized into 36 sectors, each sector representing 10°. The bottom friction is based on the JONSWAP formulation (Hasselmann et al. 1973) with friction coefficient 0.019 m^2s^{-3}. The coupling time step between SWAN and ADCIRC is 3600 s. In the global WWIII model, we are using a 0.25 degree structured grid (longitude: 0 to 360; latitude: -90 to 80.25), the explicit mode

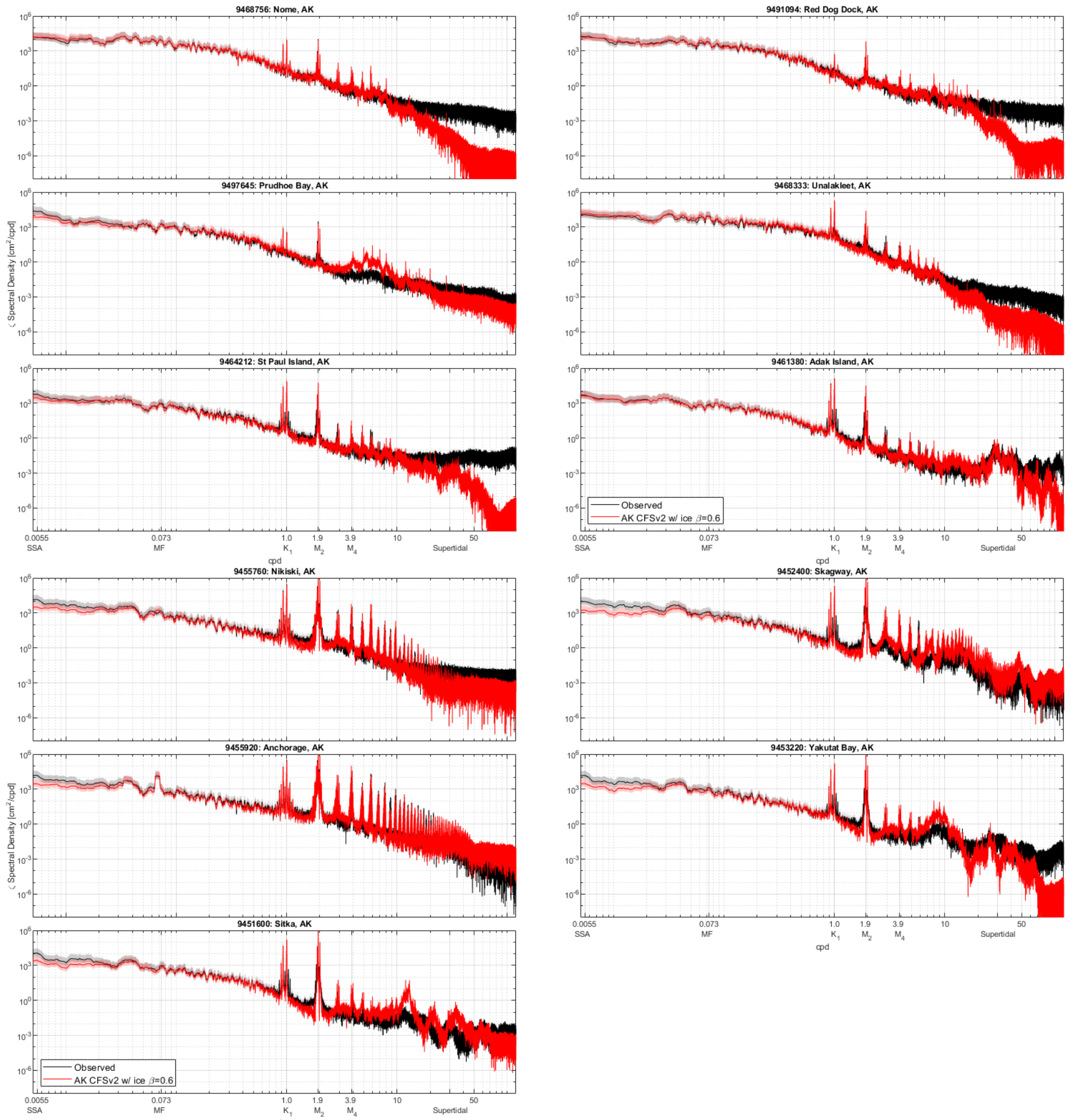

FIG. 14: Power spectral densities of 6-min sea level variations at the National Oceanic and Atmospheric Administration/National Ocean Service tide gauges in the Alaska.(cpd: cycles per day)

is applied with maximum global time step equal to 600 s, maximum CFL time step for x-y is 300 s, k-theta and minimum source term times are 450 and 10 s. The model resolves the source spectrum with frequencies from 0.042 to 0.4137 Hz, divided into 25 bins and 24 directions with

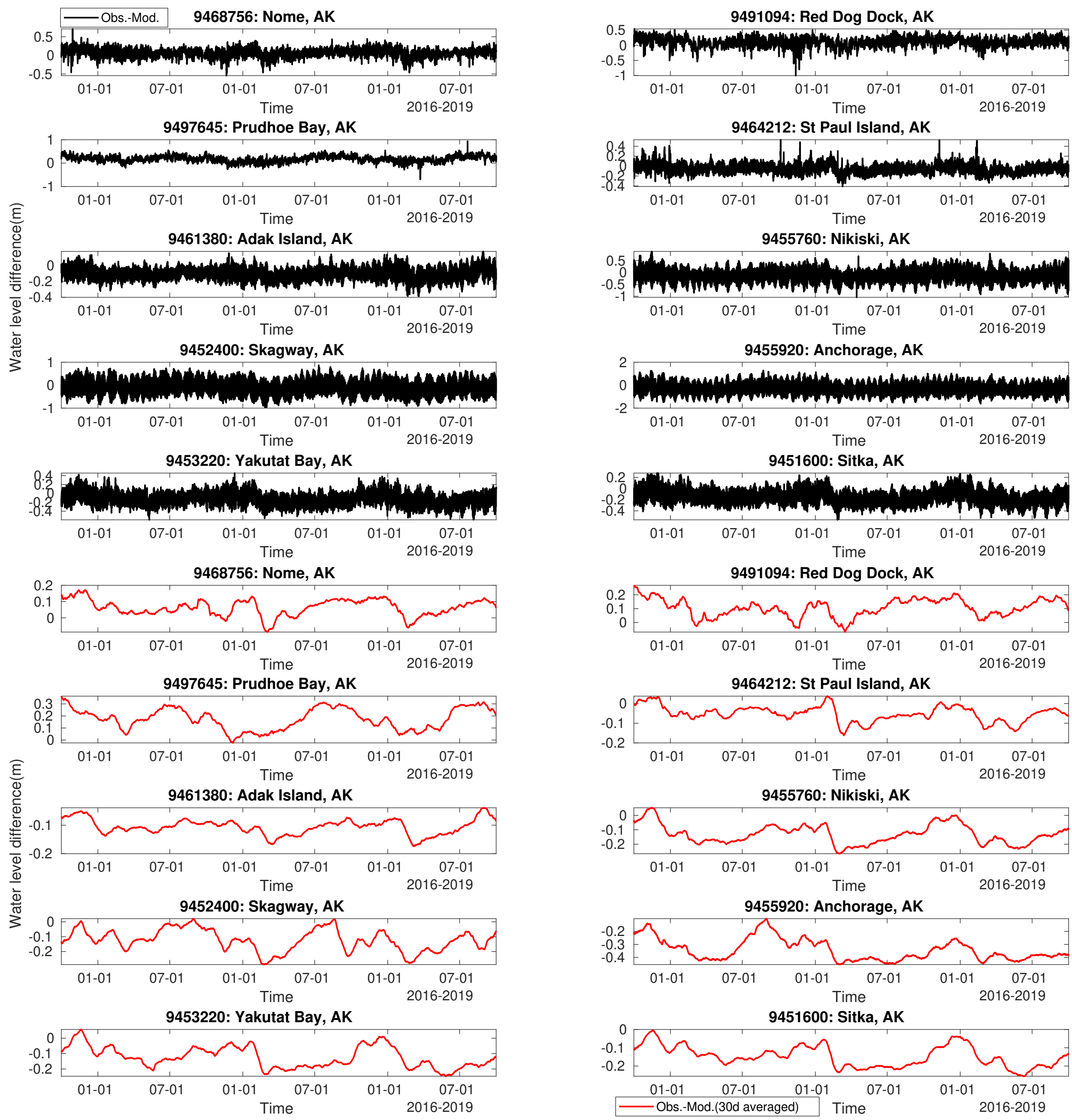

FIG. 15: Water level raw differences and after 30 day moving averaged difference between observations and model results.

15° increment. For the wave growth and dissipation, the ST4 package (Ardhuin et al. 2010) which showed good performance in Pacific Ocean (Bi et al. 2015) is employed. The IC4M2 (Meylan et al. 2014) is employed for damping waves by sea ice. The regional WWIII model is using the same unstructured mesh as SWAN+ADCIRC model, the parameters are the same as the global WW3 model, except for computational efficiency reason, the implicit time steps are chosen as 600 s. In order to consider the effect from distantly generated swell (Abdolali et al. 2020), the boundary conditions extracted from the global WWIII model are forced at the northern and southern open boundaries of the Alaska domain.

First of all, we look at the accuracy of the meteorological forcing data which is quite important for storm surge and wave models. Figs. 16-18 summarize the errors of the GFS-FV3 pressures and winds at various recorded stations with available observations for the nowcast and for various forecast periods. Here we number the stations as follows from the Gulf of Alaska to the north of the Beaufort Sea: 1. Sitka; 2. Skagway; 3. Yakutat; 4. Anchorage; 5. Nikiski; 6. Adak Island; 7. St. Paul Island; 8. Unalakleet; 9. Nome; 10. Red Dog Dock; 11. Prudhoe Bay (for the wind speed comparison in Fig.17, there are only 6 stations with data available for the comparisons). From the comparison of coefficient of determination (R^2), Normalized Root Mean Square Error (NRMSE), Average Difference between Observed and Modeled ($\bar{\epsilon}$), Averaged Absolute Difference between Observed and Modeled ($|\bar{\epsilon}|$), Standard Deviation (σ), we note that the nowcast meteorology provides the best results compared to the observations, and the error goes up the more days that we forecast into the future for all the stations. We also note that the forcing pressure from GFS-FV3 is very reliable at all the 11 stations, but that the accuracy of the wind varies and is especially poor at station 4 (Anchorage), most likely because the resolution of the wind product is not able to represent the geometry and the land/water interface around this local area. Furthermore, we note that the winds are generally much more accurate over open water based on the comparisons to measured winds at NDBC buoys (Fig. 18).

Second, in terms of validation of water levels at all 11 stations, Fig. 19 shows the comparisons of water levels from SWAN+ADCIRC nowcast results with observations at four NOAA stations (Nome, Red Dog Dock, Prudhoe Bay, Unalakleet). The water levels of the models were adjusted by a 5 days moving average difference between the model results and observations. From the figures, we can see that the results are in good agreement with the observations overall, except the water level at the Prudhoe Bay station was not able to capture the troughs due to the fact that wetting and drying in the numerical model is limited by insufficient depth related to poor model bathymetry adjacent to the station (the bathymetry around the station is only 0.5 meters deep and has been aliased). In addition, the Unalakleet station, has water levels that do not match the observation well during many periods. Again we note that the observational data is not reliable at this station throughout the year but especially during the ice season due to entrance siltation as well as ice blockages.

Fig. 20 shows the error statistics for the nowcast and forecast results compared to observational data at the 11 different stations. From the figures, we can see the model results both for the nowcast as well as for the forecasts are especially good in tidally dominated regions including stations in the Gulf of Alaska (stations 1 to 5) and in the Southern Bering Sea (stations 6 and 7). At stations on the Bering and Beaufort continental shelves where tidal ranges are much smaller and winds are especially effective storm surge drivers due to the wide and shallow continental shelves (stations 8 to 11), the forecast quality tends to deteriorate as the forecasts extend further out. Broadly, the water level forecasts still tend to have better non-dimensionalized statistics than the nearshore winds, partly due to the tidal contribution which tends to be very accurate and partly due to the fact that the GFS-FV3 winds are more accurate over water than adjacent to the land/water interface as will be shown in a subsequent section. Nonetheless the water level forecast quality clearly deteriorates with the length of the forecast as the wind forecast quality deteriorates both adjacent to the shore (as indicated by the wind stations considered here) as well over open water (as indicated by wind comparison data at NDBC buoys). We again note that station 8 (Unalakleet) is especially poor since we know that the observational data is not reliable as an indicator of nearby water levels due to inlet silting and ice jam issues.

Fig. 21 shows the validations at four representative buoys, 46001 located in the Western Gulf of Alaska, 46073 located in the Southeast Bering Sea, 46077 located in the Shelikof Strait and 46081 located in western Prince William Sound. We can see that at the buoys 46001 and 46073, where the forcing wind products are performing well compared to observations, all three wave models are also performing well in representing significant wave heights. For buoy 46077 which is located in the Shelikof Strait located between the Alaskan mainland and Kodiak Island, the global WW3 model with coarser resolution does not perform as well as the other two regional high resolution models. Furthermore, for buoy 46081 located well within Prince William Sound, the global model has no results and the area is not represented in the grid. We also note that the forcing wind is under-predicted due to the coarse resolution of the GFS-FV3 winds in comparison to the scale of the geometric complexity of the inlet, resulting in the two regional wave models both under predicting waves. At the same time, we can see the SWAN+ADCIRC gets higher waves than the WW3 model at low wind speeds. One possible reason for this difference may be the different physics source terms and parameters used in the wave models while another reason might be the SWAN+ADCIRC is a fully two way coupled system while for WW3 we are still using a stand-alone model. For future work, we will take a closer look at the difference in the physics applied in SWAN and WW3, and we are on track to fully couple WW3 with ADCIRC through NEMS (The NOAA Environmental Modeling System, Moghimi et al. (2020)).

Figs. 22-24 summarize the error statistics of the wind and significant wave height for the nowcast and forecast results of GFS-FV3, SWAN+ADCIRC, regional WW3, global WW3 models at 8 different NDBC buoys 46001, 46072, 46073, 46077, 46078, 46081, 46083 and 46084. Again, overall, we can see the errors for the forcing wind and model wave results see increasing errors from the nowcast to the first day forecast, then to the fifth day forecast. Generally we note that the offshore wind stations see smaller errors than stations at the land/ocean interface (typically NOS tide stations). The wind error at buoy 46081 is higher than at the other buoys, which results in a higher error for the nowcast and forecast results of the wave models. Furthermore, the nowcast and two day forecast results of the 3 wave models are performing well with greater than 0.85 and NRMS around 0.1 (except buoy 46081 for all and buoy 46077 for the global WW3 model).

8. Summary and conclusions

This paper has presented a high fidelity integrated sea ice, storm wave and surge Alaska coastal ocean forecast system (ALCOFS) and it has been running continuously as a preliminary real time operational forecasting system for more than one year. In the system, a targeted high resolution western Alaska storm surge model which is approximately eight times faster and as accurate as (even performs slightly better in term of tidal simulation than) a previous study model, SWAN+ADCIRC works as a main engine, and we incorporated a more complex air-sea-ice drag parameterization into ADICRC, meanwhile, the sea ice function to the interaction between SWAN and ADICRC was activated. Four storm surge events in the region on western Alaska have been examined to validate the effectiveness of the sea ice and storm wave effects to storm surge. Further more, a three year long term hindcast has been implemented to see the uncertainties about the sea level trends. Finally, we varidated the recorded forecasting results from ALCOFS with detailed observations.

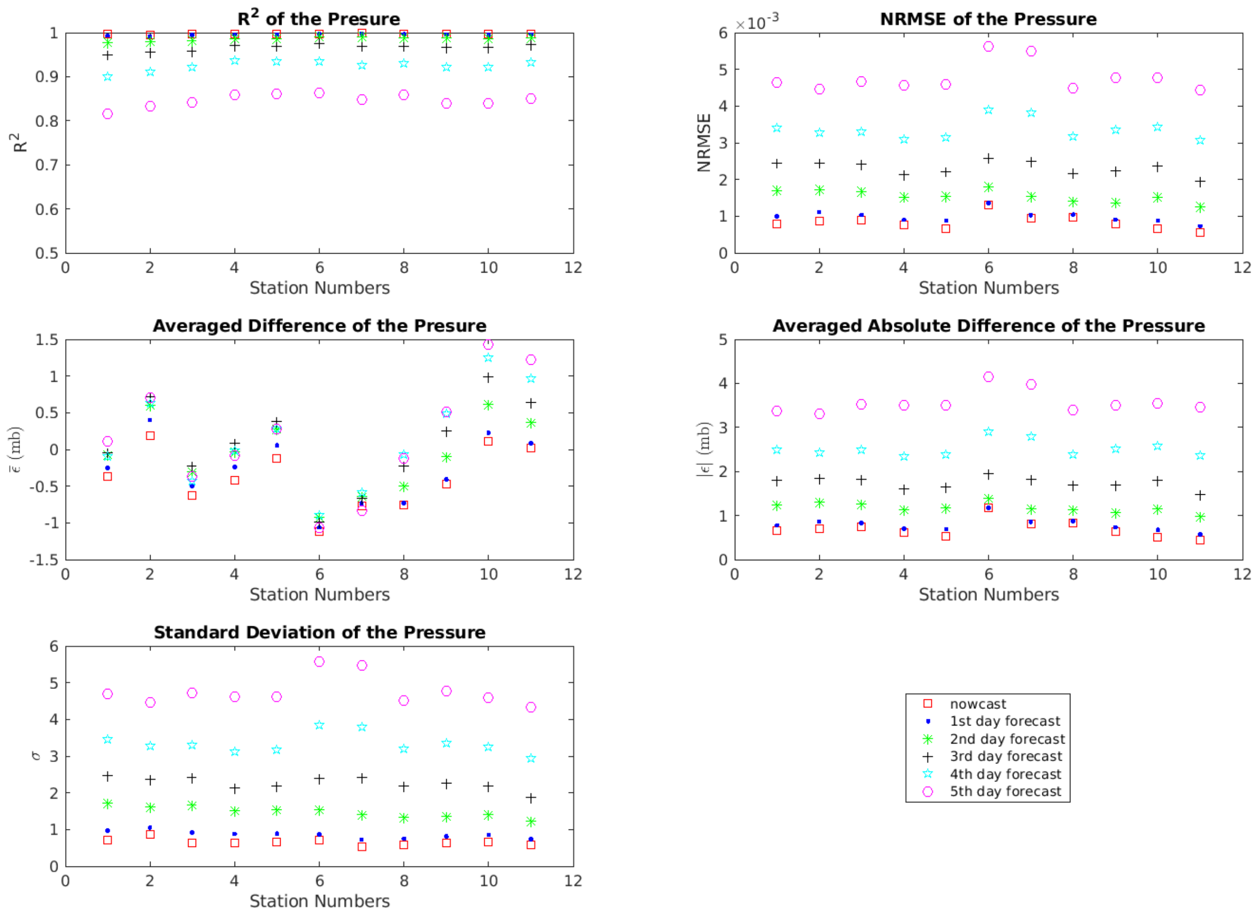

FIG. 16: Atmospheric pressure error statistic for 11 stations (1. Sitka; 2. Skagway; 3. Yakutat; 4. Anchorage; 5. Nikiski; 6. Adak Island; 7. St. Paul Island; 8. Unalakleet; 9. Nome; 10. Red Dog Dock; 11. Prudhoe Bay).

The key findings in this study are summarized as follows:

- The high targeted resolution model which put finer resolution in narrow geometric features, along steep topographic gradients, along pronounced submerged estuarine channels, and floodplains with local communities, while aggressively relaxing resolution elsewhere especially in the deep ocean area is much more efficient than a wide same high resolution in term of real time operational forecasting.

- The incorporated air-sea-ice drag parmeterization in this study showed better performance than the standard ADCIRC model without sea ice forcing, based on the error statistics compared to observations for the winter storms occurred in the northwestern Alaska with sea ice existing.

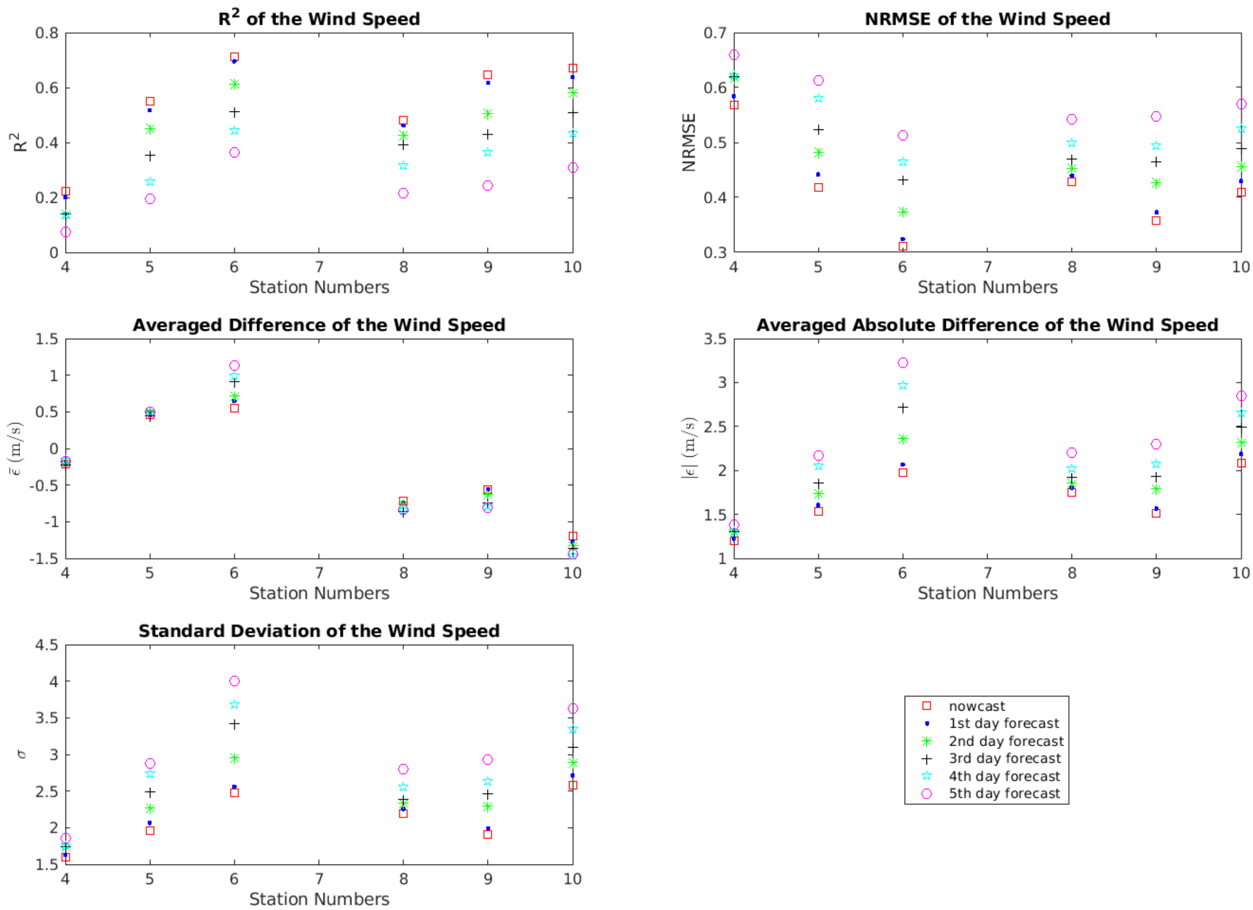

FIG. 17: Wind speed error statistic for 6 stations (4. Anchorage; 5. Nikiski; 6. Adak Island; 8. Unalakleet; 9. Nome; 10. Red Dog Dock).

By including the sea ice effect, the water level could increase maximum 30 cm at the Nome station, reduce maximum 8.04% RE compared to the model without ice forcing.

- The accuracy of the wave model highly rely on the forcing wind, when the wind is well reproduced, the significant wave height shows very good agreement with observations. From the error statistics comparison of with wave (SWAN+ADCIRC) and without wave (ADCIRC) models, the SWAN+ADCIRC model shows very similar results to the ADCIRC model for the validated stations (Nome, Red Dog Dock) during four different winter storms. However, from the comparison of water level difference between SWAN+ADCIRC and ADCIRC models, we found that, by including wave, the water elevation could increase maximum 8 cm at the Nome station, reduce 2.93% RE compared to the model without waves during the storm period with fewer sea ice coverage (Jan. 2017).

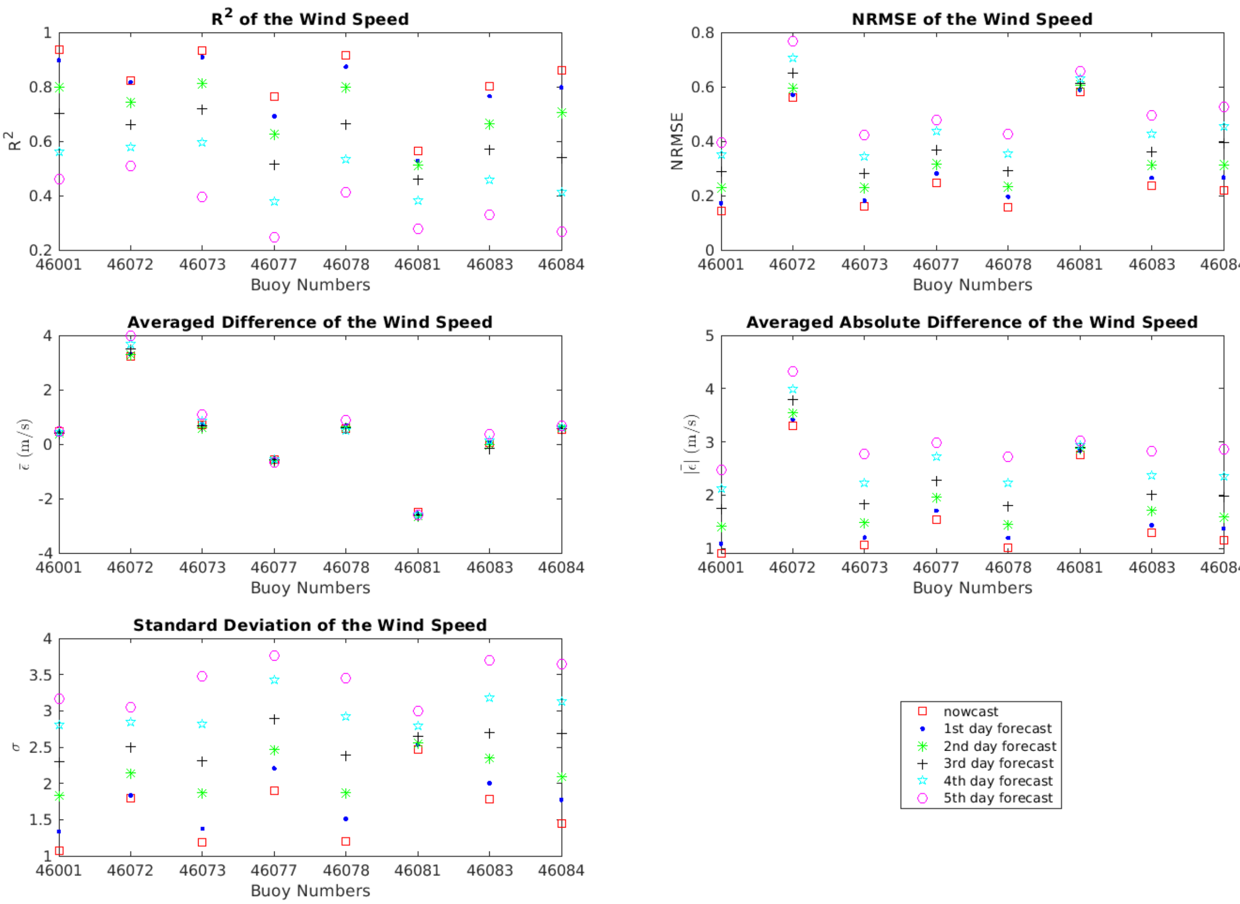

FIG. 18: Wind speed error statistic for 8 NDBC buoys with observations.

- The presented model is robust for a long term simulation, and it showed reasonable good hincast water level results compared to observations, also by looking at the power spectral densities of the 6-minute sea level variations for both our model results and the station measured signal, the model shows good matches with observations for the sub-tidal and tidal range between the M_F and M_4, but underestimated for the long term period S_{SA} which probably due to the lack of considering baroclinic (temperature or salinity etc.) effects. Also, all the stations seem to fluctuate seasonally, the offsets go up during summer then go down from February to May, likely due to the missing physics of freshwater inflows.

- The validations for the results of the past one year nowcast and forecast indicates that the forecasting results of water levels and significant wave heights are highly consistent with the observations except some problematic station (Unalakleet) and buoy (46081), the nowcast provides the best results compared to the observations, and the error goes up the more days

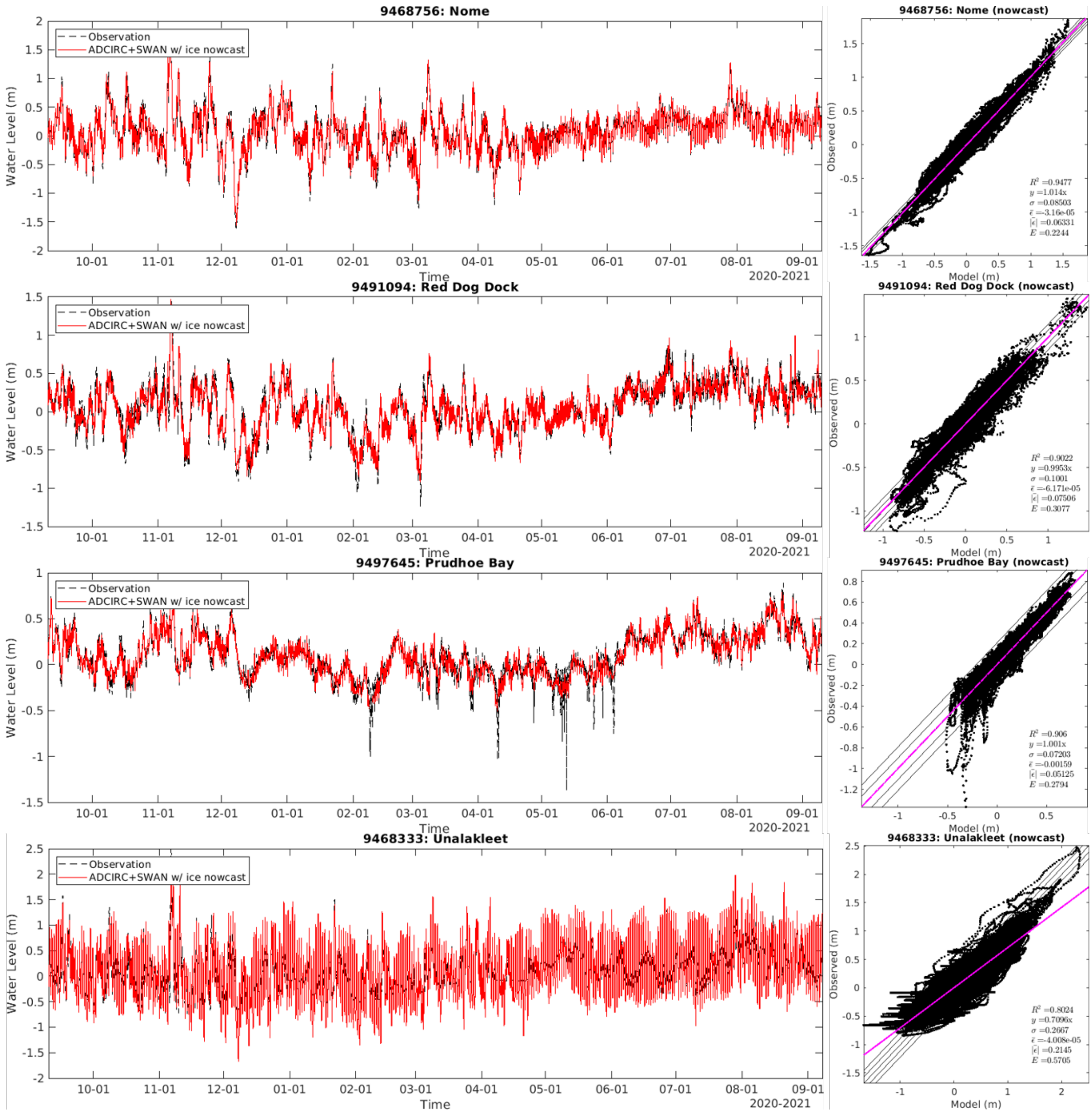

FIG. 19: Validation of water levels at four northern Alaska stations.

that we forecast into the future for all the stations, which are resulting from the forecasting forcing data.

The ALCOFS introduced in this study has showed very robustness, efficient and promising high accuracy forecast for the western Alaska region, which is promising to support marine commerce, navigational safety, marine forecasting, energy sitting and production, economic coastal

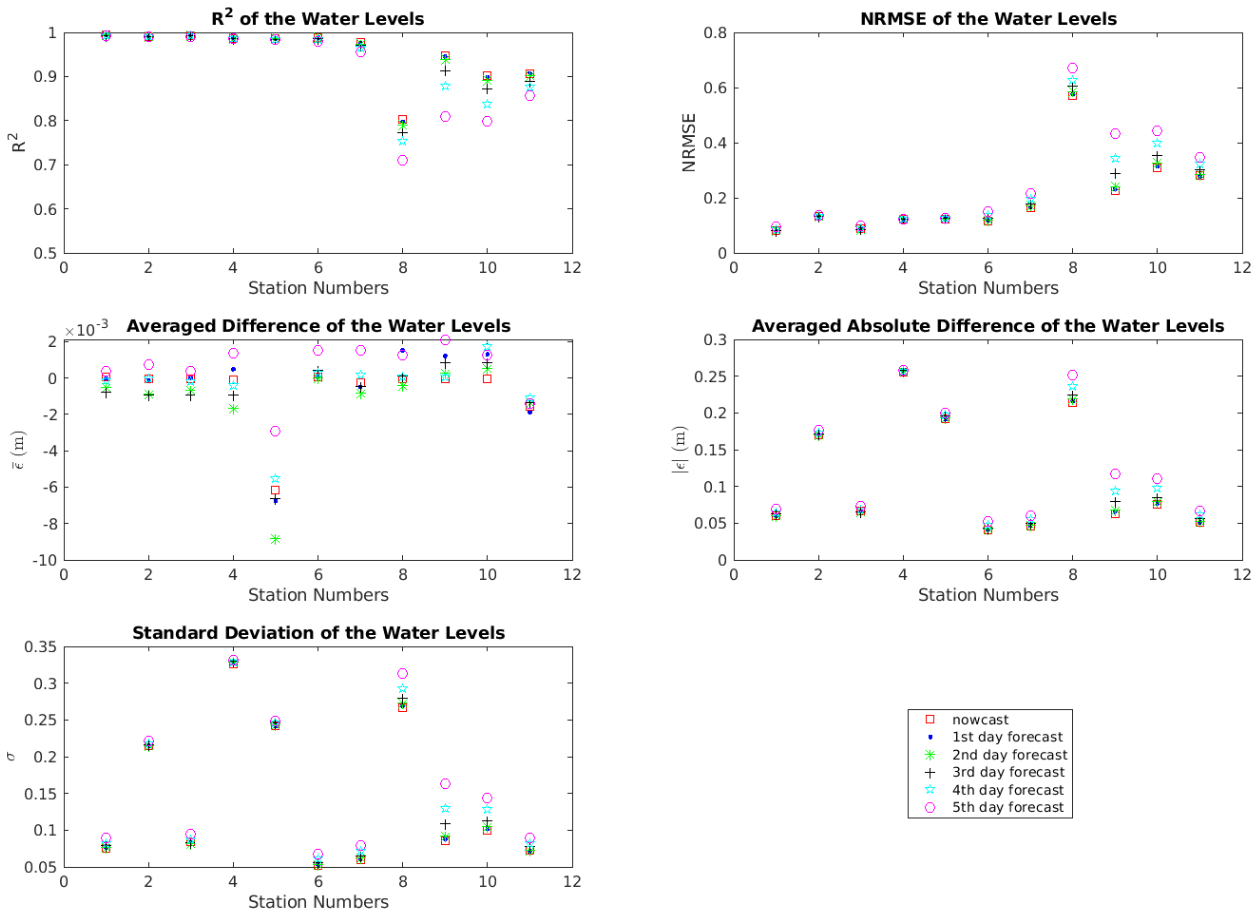

FIG. 20: Water levels error statistic (1. Sitka; 2. Skagway; 3. Yakutat; 4. Anchorage; 5. Nikiski; 6. Adak Island; 7. St. Paul Island; 8. Unalakleet; 9. Nome; 10. Red Dog Dock; 11. Prudhoe Bay).

development, and ecosystem based marine and coastal management, especially as it supports the fisheries in the region. For the future works, merging the presented operational Alaska model into a global model to run without forcing boundary conditions might potentially help to improve the current systems, and also considering the baroclinic effects to better reproduce the long term tidal constituents. Last but not least, coupling with high resolution sea ice model (CICE) and WWIII with ADICRC using ESMF (Earth System Modeling Framework) / NUOPC(National Unified Operational Prediction Capability) through NEMS (NOAA Evironmental Modeling System) application.

Acknowledgments. This work is being supported by National Oceanic and Atmospheric Administration (NOAA) for the Alaska Coastal Ocean Forecast System (ALCOFS) project.

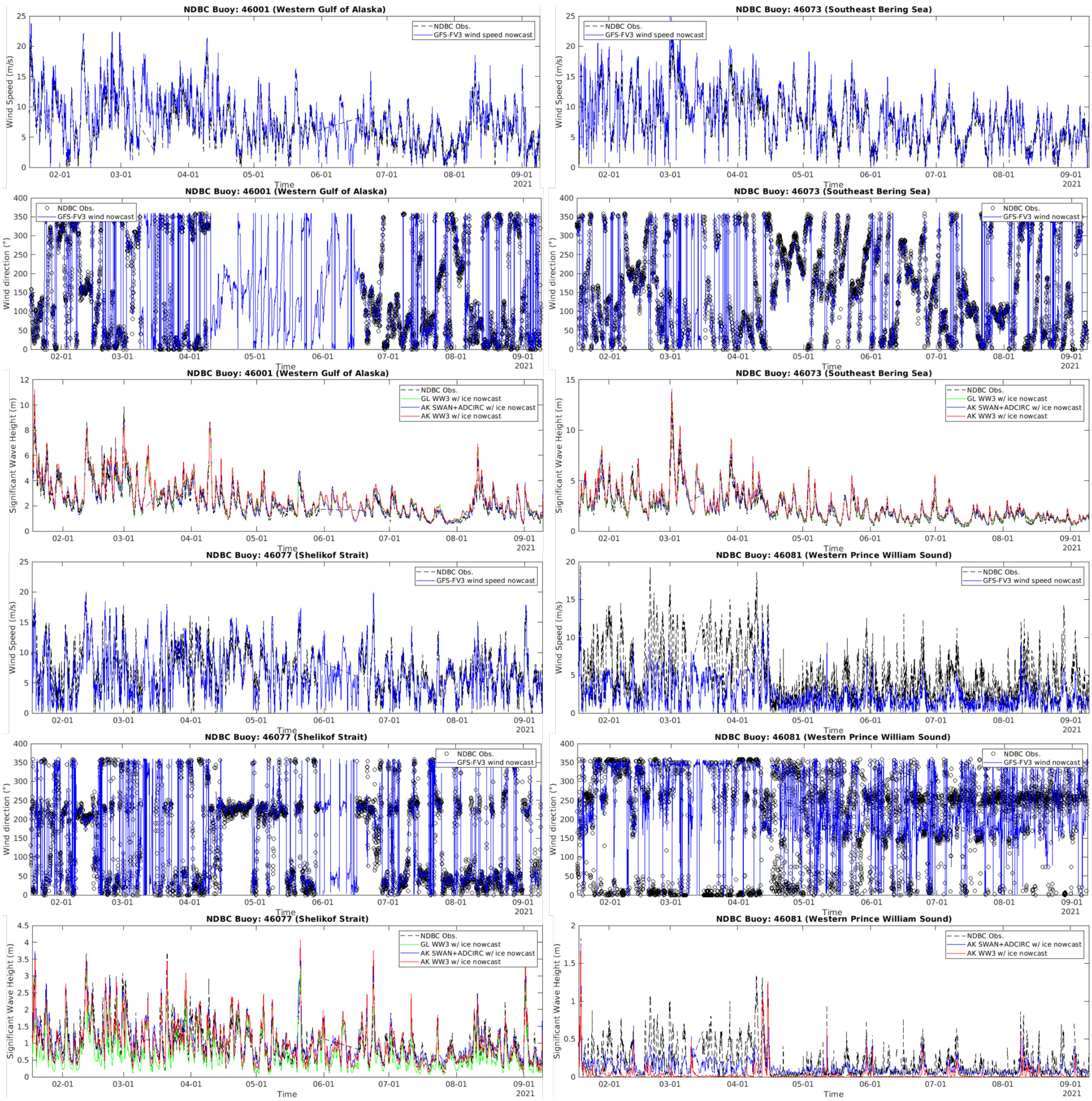

FIG. 21: Validation of wind speeds, wind directions, significant wave heights at four buoys.

APPENDIX A

Error Metrics

The Normalized Root Mean Square Error (NRMSE) is given by

$$\mathrm{NRMSE} = \sqrt{\frac{\sum(\zeta_{\mathrm{m}} - \zeta_{\mathrm{o}})^2}{\sum \zeta_{\mathrm{o}}^2}}, \tag{A1}$$

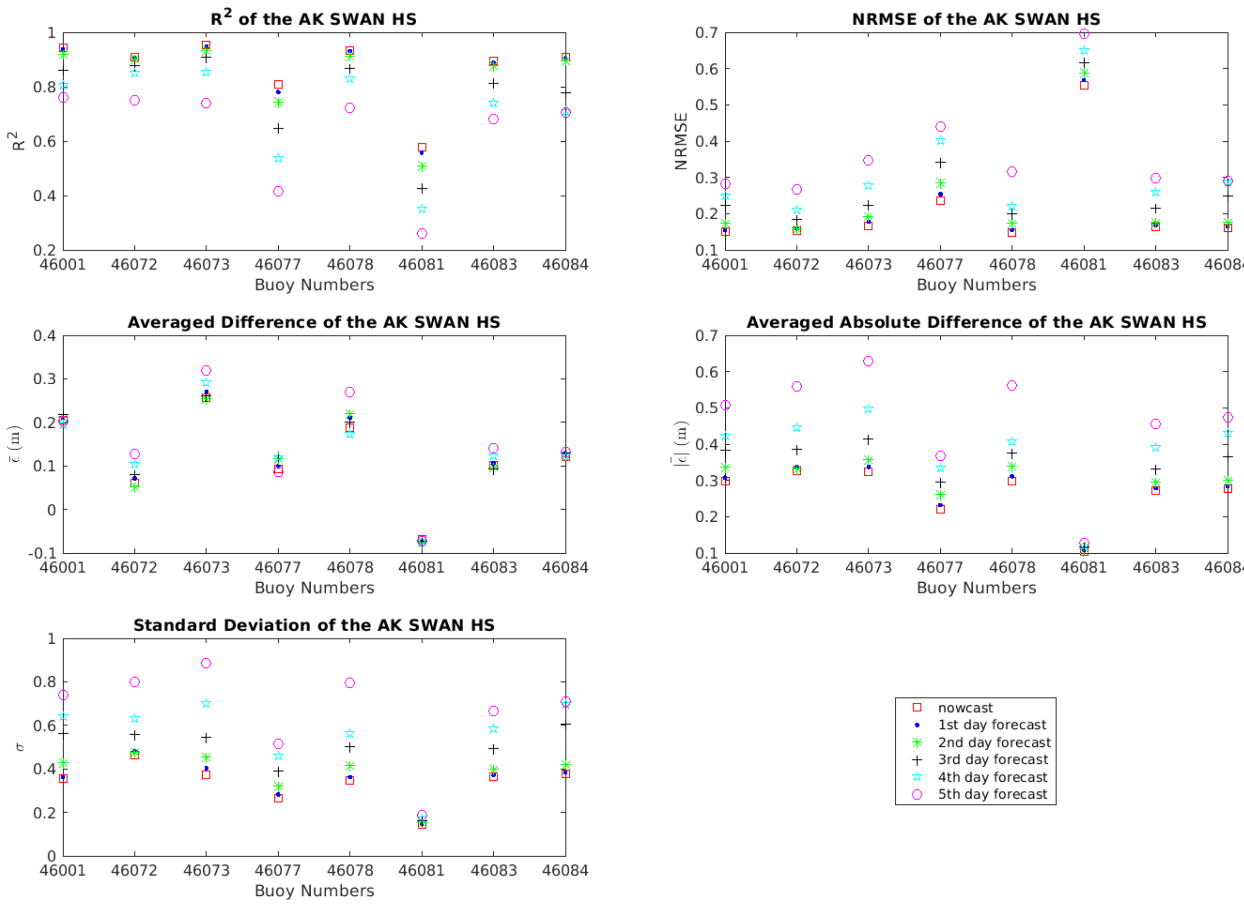

FIG. 22: Significant wave height error statistic for 8 NDBC buoys with observations.

where ζ_{m} is the model result, ζ_{o} is the observed data.

Averaged difference $\bar{\epsilon}$ is given by

$$\bar{\epsilon} = \frac{1}{N}\sum_{i=1}^{N}(\zeta_{mi} - \zeta_{oi}), \tag{A2}$$

where N is the total number of data.

Averaged absolute difference $|\bar{\epsilon}|$ is given by

$$|\bar{\epsilon}| = \frac{1}{N}\sum_{i=1}^{N}(|\zeta_{mi} - \zeta_{oi}|). \tag{A3}$$

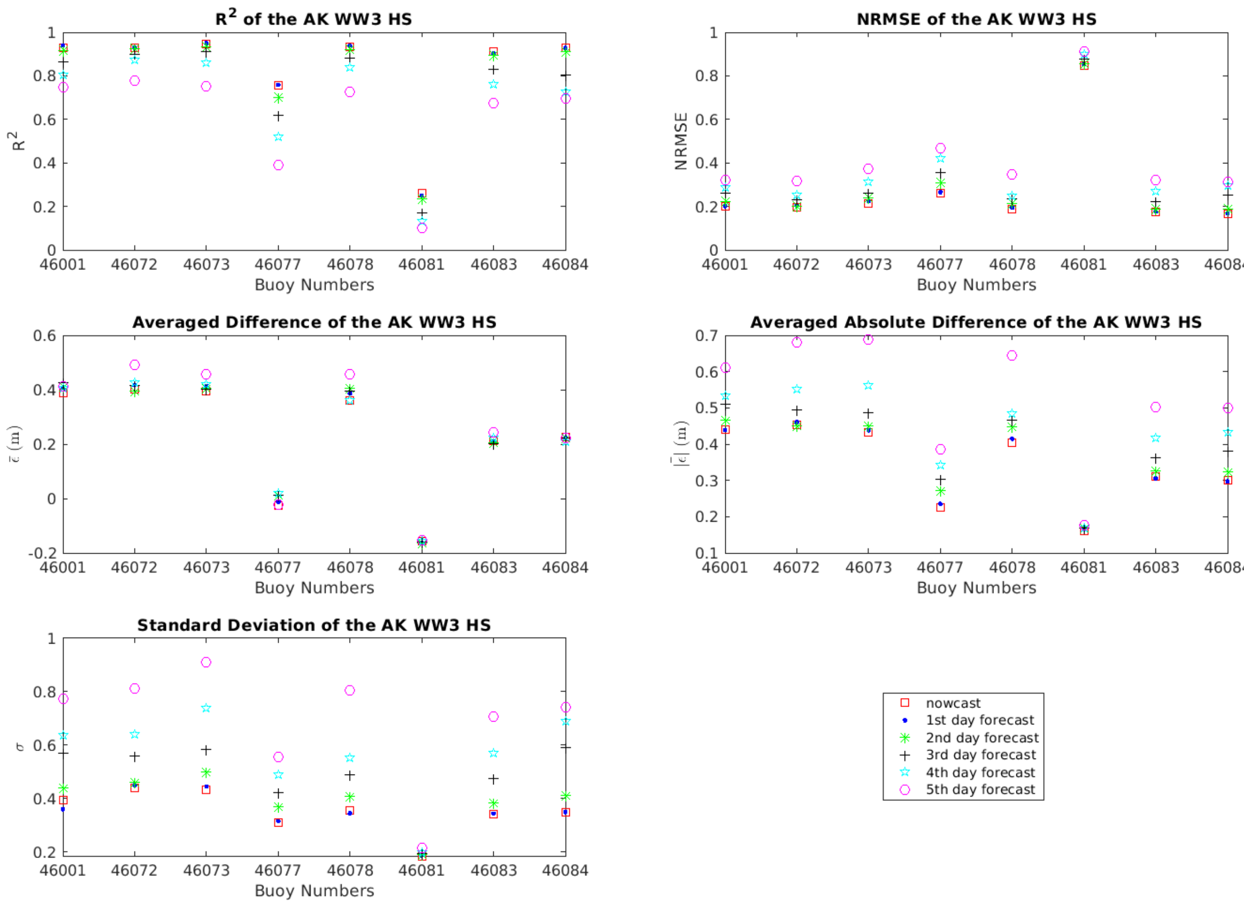

FIG. 23: Significant wave height error statistic for 8 NDBC buoys with observations.

Willmott skill score (WSS, Willmott (1981)) is given by

$$\mathrm{WSS} = 1 - \frac{\sum_{i=1}^{N}(\zeta_{mi} - \zeta_{oi})^2}{\sum_{i=1}^{N}(|\zeta_{mi} - \bar{\zeta_{oi}}| + |\zeta_{oi} - \bar{\zeta_{oi}}|)^2}. \tag{A4}$$

APPENDIX B

Performance of different β of ice drag parameterization

Table B1 shows a comparison of error statistics for using different β in the ice drag parameterization with the case not forcing ice at Nome and Red Dog Dock stations. We can see SS are improved for all the cases with ice forcing compared to the case without ice. Overall, the cases with β=0.6 turn out to perform the best especially in terms of the RE and NRMSE.

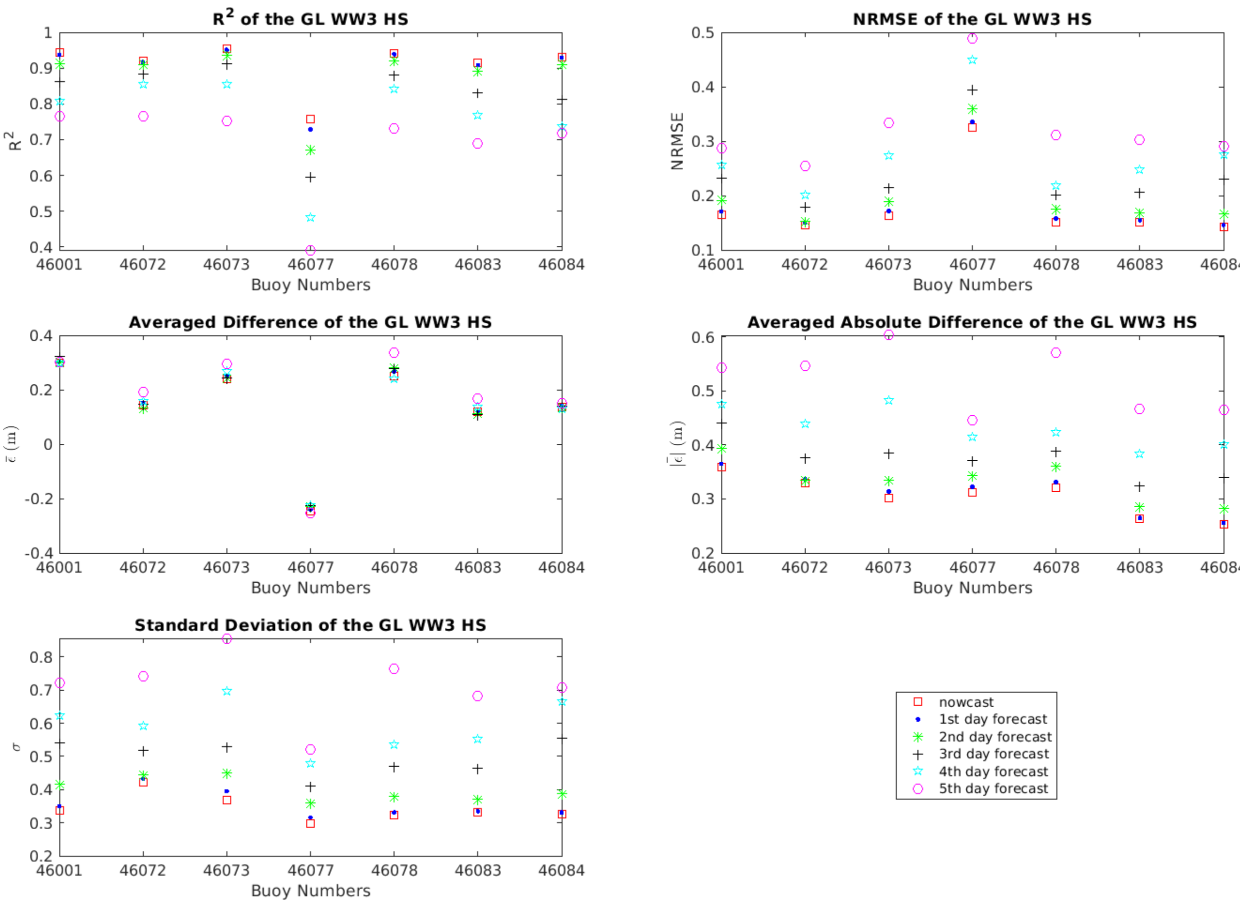

FIG. 24: Significant wave height error statistic for 8 NDBC buoys with observations.

References

Abdolali, A., A. Roland, A. van der Westhuysen, J. Meixner, A. Chawla, T. J. Hesser, J. M. Smith, and M. D. Sikiric, 2020: Large-scale hurricane modeling using domain decomposition parallelization and implicit scheme implemented in wavewatch iii wave model. *Coastal Engineering*, **157**, 103 656, doi:https://doi.org/10.1016/j.coastaleng.2020.103656.

Anderson, R., 1987: Wind stress measurements over rough ice during the 1984 marginal ice zone experiment. *Journal of Geophysical Research: Oceans*, **92**, 6933–6941, doi:https://doi.org/10.1029/JC092iC07p06933.

Andreas, E., T. Horst, A. Grachev, P. Persson, C. Fairall, P. Guest, and R. Jordan, 2010: Parametrizing turbulent exchange over summer sea ice and the marginal ice zone. *Quarterly Journal of the Royal Meteorological Society*, 927–943, url:http://hdl.handle.net/10945/47182.

Nome								
	Peak	RE	R^2	$\bar{\epsilon}$	$\lvert\bar{\epsilon}\rvert$	NRMSE	σ	SS
obs. (Feb. 2011)	1.881							
w/o ice	1.737	-7.66%	0.9468	0.0463	0.1131	0.2479	0.1312	0.9824
w/ ice β=1.0	1.7002	-9.61%	0.9556	0.0506	0.1063	0.2304	0.119	0.9851
w/ ice β=0.6	1.8698	-0.59%	0.9603	0.0794	0.1098	0.2441	0.1116	0.9847
w/ ice β=0.3	2.1356	13.54%	0.959	0.1286	0.1516	0.3499	0.1484	0.9728
obs. (Jan. 2017)	2.205							
w/o ice	1.9315	-12.40%	0.9686	-0.0519	0.1082	0.2249	0.1325	0.984
w/ ice β=1.0	2.097	-4.90%	0.9772	-0.0451	0.0833	0.164	0.0935	0.9924
w/ ice β=0.6	2.1088	-4.36%	0.9758	-0.0437	0.0835	0.1650	0.0948	0.9924
w/ ice β=0.3	2.1091	-4.35%	0.9755	-0.0428	0.0835	0.1653	0.0954	0.9924
Red Dog Dock								
	Peak	RE	R^2	$\bar{\epsilon}$	$\lvert\bar{\epsilon}\rvert$	NRMSE	σ	SS
obs. (Feb. 2011)	2.106							
w/o ice	1.7861	-15.19%	0.9387	-0.0134	0.0971	0.2387	0.1217	0.9826
w/ ice β=1.0	1.7554	-16.65%	0.9372	-0.003	0.0964	0.2382	0.1221	0.9829
w/ ice β=0.6	1.9204	-8.81%	0.9376	0.022	0.0999	0.2454	0.1239	0.9833
w/ ice β=0.3	2.1395	1.59%	0.9447	0.0597	0.1186	0.2961	0.1397	0.9784
obs. (Jan. 2017)	1.928							
w/o ice	1.3935	-27.72%	0.9042	-0.1113	0.1639	0.3578	0.1619	0.962
w/ ice β=1.0	1.5742	-18.35%	0.9006	-0.1059	0.1725	0.3713	0.1742	0.9637
w/ ice β=0.6	1.6111	-16.44%	0.9077	-0.1041	0.1681	0.3633	0.1701	0.9657
w/ ice β=0.3	1.6051	-16.75%	0.9122	-0.1028	0.1627	0.3528	0.1627	0.9673

TABLE B1: Comparisons of water levels (m) between the observations and model simulations for 2 storms at Nome and Red Dog Dock stations.

Andreas, E. L., W. B. T. III, and S. F. Ackley, 1984: Atmospheric boundary-layer modification, drag coefficient, and surface heat flux in the antarctic marginal ice zone. *Journal of Geophysical Research: Oceans*, **89**, 649–661, doi:https://doi.org/10.1029/JC089iC01p00649.

Ardhuin, F., and Coauthors, 2010: Semiempirical dissipation source functions for ocean waves. part i: Definition, calibration, and validation. *Journal of Physical Oceanography*, **40**, 1917–1941, doi:https://doi.org/10.1175/2010JPO4324.1.

Bi, F., J. Song, K. Wu, and Y. Xu, 2015: Evaluation of the simulation capability of the wavewatch iii model for pacific ocean wave. *Acta Oceanologica Sinica*, **34**, 43–57, doi:https://doi.org/10.1007/s13131-015-0737-1.

Blier, W., S. Keefe, W. A. Shaffer, and S. C. Kim, 1997: Storm surges in the region of western alaska warren. *Monthly Weather Review*, **125**, 3094–3108, doi:https://doi.org/10.1175/1520-0493(1997)125<3094:SSITRO>2.0.CO;2.

Booij, N., R. Ris, and L. Holthuijsen, 1999: A third-generation wave model for coastal regions 1. model description and validation. *Journal of Geophysical Research: Oceans*, **104**, 7649–7666, doi:https://doi.org/10.1029/98JC02622.

Collins, C. O., and W. E. Rogers, 2017: A source term for wave attenuation by sea ice in wavewatch iii®: Ic4. https://www7320.nrlssc.navy.mil/pubs/2017/rogers-2017.pdf.

Dietrich, J., and Coauthors, 2011: Modeling hurricane waves and storm surge using integrally-coupled, scalable computations. *Coastal Engineering*, **58**, 45–65, doi:https://doi.org/10.1016/j.coastaleng.2010.08.001.

Dietrich, J., and Coauthors, 2012: Performance of the unstructured-mesh, swan+ adcirc model in computing hurricane waves and surge. *Journal of Scientific Computing*, **52**, 468–497, doi:https://doi.org/10.1007/s10915-011-9555-6.

Egbert, G. D., and S. Y. Erofeeva, 2002: Efficient inverse modeling of barotropic ocean tides. *Journal of Atmospheric and Oceanic Technology*, **19**, 183–204, doi:https://doi.org/10.1175/1520-0426(2002)019<0183:EIMOBO>2.0.CO;2.

Fathauer, T. F., 1975: The great bering sea storms of 9–12 november 1974. *Weatherwise*, **28**, 76–83, doi:https://doi.org/10.1080/00431672.1975.9931740.

Garratt, J. R., 1977: Review of drag coefficients over oceans and continents. *Monthly Weather Review*, **105**, 915–929, doi:https://doi.org/10.1175/1520-0493(1977)105<0915:RODCOO>2.0.CO;2.

Guest, P., and K. Davidson, 1987: The effect of observed ice conditions on the drag coefficient in the summer east greenland sea marginal ice zone. *Journal of Geophysical Research: Oceans*, **92**, 6943–6954, doi:https://doi.org/10.1029/JC092iC07p06943.

Hasselmann, K., and Coauthors, 1973: Measurements of wind–wave growth and swell decay during the joint north sea wave project (jonswap). *Ergnzungsheft zur*

Deutschen Hydrographischen Zeitschrift Reihe 12 (A8), http://resolver.tudelft.nl/uuid:f204e188-13b9-49d8-a6dc-4fb7c20562fc.

Joyce, B. R., W. J. Pringle, D. Wirasaet, J. J. Westerink, A. J. V. der Westhuysen, R. Grumbine, and J. Feyenc, 2019: High resolution modeling of western alaskan tides and storm surge under varying sea ice conditions. *Ocean Modelling*, **141**, 101 421, doi:https://doi.org/10.1016/j.ocemod.2019.101421.

Kinsman, N. E., and M. R. DeRaps, 2012: Coastal hazard field investigations in response to the november 2011 bering sea storm, norton sound, alaska. *Alaska DNR, Division of Geological and Geophysical Surveys Report*, https://dggs.alaska.gov/webpubs/dggs/ri/text/ri2012_002.pdf.

Kolar, R. L., W. G. Gray, J. J. Westerink, and R. A. L. Jr., 1994: Shallow water modeling in spherical coordinates: Equation formulation, numerical implementation, and application. *Journal of Hydraulic Research*, **32**, 1–24, doi:https://doi.org/10.1080/00221689409498786.

Li, A., S. Guan, D. Mo, Y. Hou, X. Hong, and Z. Liu, 2020: Modeling wave effects on storm surge from different typhoon intensities and sizes in the south china sea. *Estuarine, Coastal and Shelf Science*, **235**, 106 551, doi:https://doi.org/10.1016/j.ecss.2019.106551.

Lim, E., B. Eakins, and R. Wigley, 2011: Coastal relief model of southern alaska: Procedures, data sources and analysis. *NOAA Technical Memorandum NESDIS NGDC*, **43**, 22p, url:https://www.ngdc.noaa.gov/mgg/dat/dems/regional_tr/crm_southak.pdf.

Lüpkes, C., and G. Birnbaum, 2005: Surface drag in the arctic marginal sea-ice zone: A comparison of different parameterisation concepts. *Boundary-Layer Meteorology*, **117**, 179–211, doi:https://doi.org/10.1007/s10546-005-1445-8.

Lüpkes, C., V. M. Gryanik, J. Hartmann, and E. LAndreas, 2012: A parametrization, based on sea ice morphology, of the neutral atmospheric drag coefficients for weather prediction and climate models. *Journal of Geophysical Research Atmospheres*, **117**, D13 112, doi:https://doi.org/10.1029/2012JD017630.

Meylan, M. H., L. G. Bennetts, and A. L. Kohout, 2014: In situ measurements and analysis of ocean waves in the antarctic marginal ice zone. *Geophysical Research Letters*, **41**, 5046–5051, doi:https://doi.org/10.1002/2014GL060809.

Moghimi, S., and Coauthors, 2020: Development of an esmf based flexible coupling application of adcirc and wavewatch iii for high fidelity coastal inundation studies. *Journal of Marine Science and Engineering*, **8(5)**, 308, doi:https://doi.org/10.3390/jmse8050308.

Parker, B. B., 2007: Tidal anlysis and prediction. *NOAA Special Publication NOS CO-OPS 3*, doi:http://dx.doi.org/10.25607/OBP-191.

Prescott, M. M., and M. Zimmermann, 2015: Smooth sheet bathymetry of norton sound. *NOAA technical memorandum NMFS-AFSC*, **298**, 23p, doi:http://doi.org/10.7289/V5V69GJ9.

Pringle, W. J., J. Gonzalez-Lopez, B. R. Joyce, J. J. Westerink, and A. J. van der Westhuysen, 2019: Baroclinic coupling improves depth-integrated modeling ofcoastal sea level variations around puerto rico and the u.s. virgin islands. *Journal of Geophysical Research: Oceans*, **124**, 2196–2217, doi:https://doi.org/10.1029/2018JC014682.

Pringle, W. J., D. Wirasaet, K. J. Roberts, and J. J. Westerink, 2021: Global storm tide modeling with adcirc v55: Unstructured mesh design and performance. *Geoscientific Model Development Discussions*, **14**, 1125–1145, doi:https://doi.org/10.5194/gmd-14-1125-2021.

Provost, C. L., and F. Lyard, 2003: The impact of ocean bottom morphology on the modelling of long gravity waves from tides and tsunami to climate. *GEBCO Centenary Conference*, 25, https://www.gebco.net/about_us/presentations_and_publications/documents/cen_conf_abstract_le_provost.pdf.

Roberts, K. J., W. J. Pringle, and J. J. Westerink, 2019a: Oceanmesh2d 1.0: Matlab-based software for two-dimensional unstructured mesh generation in coastal ocean modeling. *Geoscientific Model Development*, **12**, 1847–1868, doi:https://doi.org/10.5194/gmd-12-1847-2019.

Roberts, K. J., W. J. Pringle, J. J. Westerink, M. T. Contreras, and D. Wirasaet, 2019b: On the automatic and a priori design of unstructured mesh resolution for coastal ocean circulation models. *Ocean Modelling*, **44**, 101 509, doi:https://doi.org/10.1016/j.ocemod.2019.101509.

Rogers, W. E., 2019: Implementation of sea ice in the wave model swan. https://www7320.nrlssc.navy.mil/pubs/2019/rogers2-2019.pdf.

Saha, S., and Coauthors, 2014: The ncep climate forecast system version 2. *Journal of Climate J. Climate*, **27**, 2185–2208, doi:https://doi.org/10.1175/JCLI-D-12-00823.1.

Savage, A. C., and Coauthors, 2017: Frequency content of sea surface height variability from internal gravity waves to mesoscale eddies. *Journal of Geophysical Research: Oceans*, **122**, 2519–2538, doi:https://doi.org/10.1002/2016JC012331.

Schröder, D., T. Vihma, A. Kerber, and B. Brümmer, 2003: On the parameterization of turbulent surface fluxes over heterogeneous sea ice surfaces. *Journal of Geophysical Research: Oceans*, **108**, 3195, doi:https://doi.org/10.1029/2002JC001385.

Thomson, D. J., 1982: Spectrum estimation and harmonic analysis. *Proceedings of the IEEE*, **70**, 1055–1096, doi:https://doi.org/10.1109/PROC.1982.12433.

Weaver, R., and D. Slinn, 2010: Influence of bathymetric fluctuations on coastal storm surge. *Coastal Engineering*, **57**, 62–70, doi:https://doi.org/10.1016/j.coastaleng.2009.09.012.

Westerink, J. J., and Coauthors, 2008: A basin- to channel-scale unstructured grid hurricane storm surge model applied to southern louisiana. *Monthly Weather Review*, **136**, 833–864, doi:https://doi.org/10.1175/2007MWR1946.1.

Willmott, C. J., 1981: On the validation of models. *Physical Geography*, **2:2**, 184–194, doi:https://doi.org/10.1080/02723646.1981.10642213.

WW3DG, 2019: User manual and system documentation of WAVEWATCH III version 6.07, the WAVEWATCH III development group. *Tech. Note 326 pp. + Appendices, NOAA/NWS/NCEP/MMAB*, https://www.researchgate.net/publication/336069899_User_manual_and_system_documentation_of_WAVEWATCH_III_R_version_607.

Xie, D., Q. Zhou, and J. W. Cannon, 2016: Application of swan+adcirc to tide-surge and wave simulation in gulf of maine during patriot's day storm. *Water Science and Engineering*, **9**, 33–41, doi:https://doi.org/10.1016/j.wse.2016.02.003.

Zimmermann, M., and M. M. Prescott, 2014: Smooth sheet bathymetry of cook inlet, alaska. *NOAA technical memorandum NMFS-AFSC*, **275**, 32p, url:https://repository.library.noaa.gov/view/noaa/4686.

Zimmermann, M., and M. M. Prescott, 2015: Smooth sheet bathymetry of the central gulf of alaska. *NOAA technical memorandum NMFS-AFSC*, **287**, 54p, doi:http://doi.org/10.7289/V5GT5K4F.

Zimmermann, M., M. M. Prescott, and C. N. Rooper, 2013: Smooth sheet bathymetry of the aleutian islands. *NOAA technical memorandum NMFS-AFSC*, **250**, 43p, url:https://repository.library.noaa.gov/view/noaa/4426.